Can a dual pulsed lidar system measure the lateral coherence of turbulence?

Paulius Kavaliauskas

Thesis for Master of Science Degree at the University of Bergen, Norway

2023

Year: 2023
Title: Can a dual pulsed lidar system measure the lateral coherence of turbulence?
Author: Paulius Kavaliauskas

Acknowledgements

I would like to express my sincere gratitude to my main supervisor, Etienne Cheynet, for his unwavering support, valuable insights, and guidance throughout the entire thesis writing process. I am truly grateful for his constant availability and thoughtful comments, which have significantly enhanced the quality of my work. Without his guidance, I would not have gained such a deep understanding of the field. Thank you for always being there for me.

I would also like to extend my thanks to my co-supervisor, Joachim Reuder, for his help and valuable feedback. His input and expertise have greatly enriched my research, and I am grateful for his thoughtful comments and suggestions.

Additionally, I would like to express my gratitude to the Geophysical Institute for their support throughout my master's journey and for their provision of free coffee machines in the institute.

Lastly, I want to thank my family for their support and encouragement.

Abstract

Characterizing the coherence of turbulence in the marine boundary layer faces a significant challenge due to the limited availability of offshore measurements within the relevant altitude ranges, particularly up to 250 m. The coherence of turbulence describes the spatial correlation of wind velocity fluctuations, which is a key parameter for determining environmental loading on wind turbines.

The turbulent wind loading represents one of the main uncertainties faced by the offshore wind engineering sector. Uncertainties arising from turbulent wind loading represent major challenges in the offshore wind engineering sector. Advancements in remote sensing technology, such as Doppler wind lidars, have opened new possibilities for studying wind turbulence at heights relevant to the increasing size of wind turbine rotors. This master's thesis presents an analysis of 15 days of wind records collected by two pulsed wind lidars and two sonic anemometers during the COTUR project at Obrestad lighthouse, located on the southwestern coast of Norway. The site is expected to predominantly represent offshore conditions.

The primary objective of this study is to assess the capability of pulsed Doppler wind lidar instruments in capturing the lateral co-coherence of turbulence along the wind component. Wind records obtained by the sonic anemometers mounted on 11 m high masts are used as reference data. The analysis focuses on both single and two-point statistics of wind turbulence, with particular emphasis on studying the co-coherence of turbulence.

The results revealed that wind sectors aligned with northerly or southerly wind directions are suitable for comparison studies. In these wind directions, a good agreement is found between the two different instruments. Comparing co-coherence estimates obtained from pulse lidar and sonic anemometer showed negligible differences, indicating that spatial averaging did not significantly affect the estimation of co-coherence. By assessing the ability of pulsed Doppler wind lidar instruments to capture turbulence co-coherence, this study contributes to the applicability of lidar technology for characterizing turbulence and its potential for improving assessments of environmental loading on offshore wind turbines

Contents

Chapter 1

Introduction

Since the 2010s, the offshore wind energy (OWE) industry has significantly developed in Europe. The European Union aims to install 300 GW of offshore wind power by 2050. Norway has the second highest OWE potential in the world (Bosch et al., 2018) and could take 16% of the European OWE market share by 2050 while ensuring a successful transition from the oil & gas sector to the OWE sector. By that time, OWE may become a cornerstone of the European energy system and play a key role in the energy transition.

The lack of knowledge about environmental loading on wind turbines is one of the main challenges (Veers et al., 2019) faced by the OWE sector. In particular, the turbulent wind loading represents one of the main uncertainties. This thesis, therefore, focuses on the coherence of turbulence, which partly governs the dynamic wind load on large structures such as wind turbines. The coherence of turbulence is a measure of the three-dimensional correlation of the velocity fluctuations in the incoming wind field (Panofsky & McCormick, 1954) and is one of the key variables for determining wind loads on large structures (Cheynet et al., 2021).

The characterization of lateral wind coherence above land has been previously obtained from arrays of met-masts since 1970 (Ropelewski et al., 1973; Pielke & Panofsky, 1970). In recent years, remote sensing of wind with Doppler wind lidars has opened a new possibility to study the coherence of turbulence. However, despite the growing adoption of pulsed lidar technology in the meteorology and wind energy industries, there are still several challenges and limitations that need to be addressed.

To the best of the author's knowledge, no previous studies have conducted direct comparisons of pulsed wind lidar and sonic anemometer for coherence measurements. Therefore, this thesis aims to validate the wind measurements accuracy obtained by two different instruments. This assessment involves comparing the measurements obtained from the 3D ultrasonic anemometers

and the scanning long-range pulsed wind lidars.

This study is based on wind data collected during the COTUR (Coherence of Turbulence) campaign, which took place in a coastal area near Obrestad lighthouse in southwest Norway (Cheynet et al., 2021). During the campaign, a specific time period was assigned to collect wind data using two of the three land-based scanning wind lidars and two masts, equipped with 3D sonic anemometer sensors. The data collection started on March 16, 2020, and concluded on March 30, 2020.

Despite the potential effect of the terrain on the local flow conditions and limited data duration, the results for specific wind speed and directions demonstrate that Lidar measurements have a good agreement with sonic anemometer measurements.

1.1 Motivation and Contribution

In recent years, a wind turbine with a rotor diameter of up to 252 meters has been developed, reflecting the trend of increasing rotor diameters in the OWE industry. Dimension change in the rotor size challenges the traditional modeling of the coherence where mostly the arrays of onshore meteorological masts measurements are used, and typically not covering the full spatial area of modern wind turbines. According to Cheynet et al. (2021), one of the major challenges for OWE research has been recognized as a lack of data coverage at altitudes relevant to offshore wind turbines, namely 50 to 200 meters above sea level (asl).

The study is motivated by seeking alternative and accessible methods to measure the coherence of turbulence. Therefore, the current challenge arises for a measurement approach that enables remote wind assessment providing the flexibility to adjust measurement altitudes and horizontal separations. Dual pulsed lidar systems have the potential to provide a solution to this problem.

Similar investigations have been carried out for continuous wave lidar systems (Cheynet et al., 2016), but the application of long-range pulsed wind lidar in this specific context remains largely unexplored. Although dual pulsed lidar systems have demonstrated their efficacy in measuring turbulence intensity (Cheynet et al., 2018a), their capability to accurately measure coherence is still unvalidated.

Therefore, this research will pave the way for more accurate advancements in the field of wind turbine design and maintenance, facilitating the transition to sustainable energy sources.

1.2 Problem Statement and Objectives

The problem addressed in this thesis is the research gap in assessing the effectiveness of pulsed lidar in capturing the coherence of turbulence, specifically for the along-beam component. To address this knowledge gap and contribute to reducing the uncertainties, this thesis examines *validation of the ability of pulsed Doppler wind lidar instruments to capture the lateral co-coherence of turbulence.*

Wind data collected during the COTUR project provides measurements over different topographic terrains, including flat and elevated relief, as well as ocean surfaces. Different terrains can affect wind patterns, resulting in variations in wind speed, direction, and induced turbulence. Wind turbulence statistics represent one of the largest uncertainties in wind resource assessment and wind energy forecasting. This raises actually a more specific question for wind lidar: *whether highly turbulent flow, generated by the buildings around the masts can prevent the study of turbulence by the dual lidar system?*

1.3 Thesis outline

The thesis is structured into several key sections, each contributing to a comprehensive understanding of turbulence analysis using lidar remote sensing and sonic anemometer data. The first section of the thesis focuses on providing a thorough state-of-the-art review of lidar remote sensing of turbulence, which serves as a foundation for the subsequent research. The thesis then focuses on characterizing local turbulence characteristics using sonic anemometer data, identifying factors that influence turbulence under different wind directions at the site. The next step in the thesis involves calculating co-coherence using only sonic anemometer data, based on 10-minute time series. To assess the impact of local turbulence on the co-coherence measurements in different wind directions. To evaluate the reliability of scanning wind lidar measurements, the fourth part of the thesis focuses on synchronizing sonic anemometer data with scanning wind lidar data. The objective is to determine whether scanning wind lidar measurements are affected by local turbulence to a similar extent or if their reliability differs in selected wind direction in comparison to sonic anemometer data. Finally, the thesis presents the findings and conclusions under specific wind conditions and directions. It highlights the ability of scanning wind lidar to capture co-coherence under those specific wind conditions, while also emphasizing the potential underestimation of co-coherence due to measurement noise.

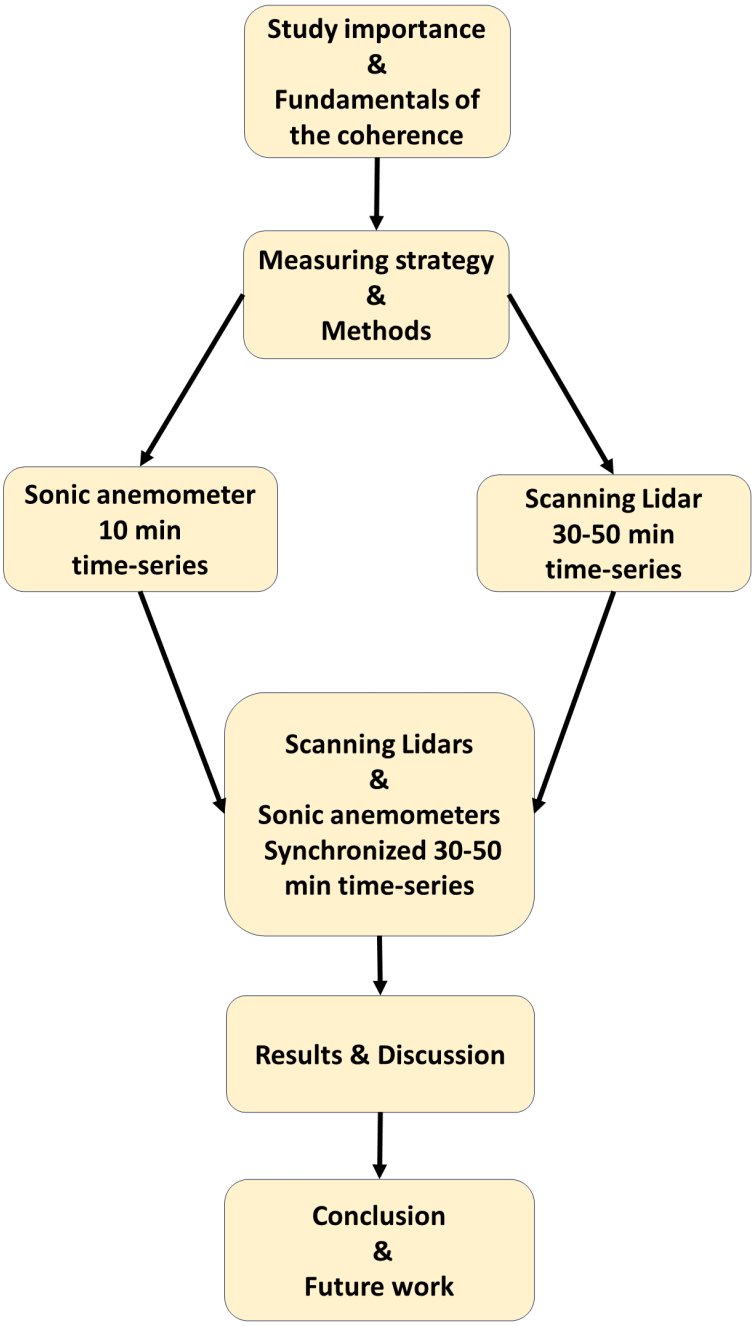

Figure 1.1: Thesis outline

Chapter 2

Background

In wind turbine design and operation, understanding turbulence is crucial for accurately assessing wind conditions and estimating the loads experienced by wind turbines. Wind turbulence refers to the chaotic and irregular motion of the fluid flow, leading to fluctuations in wind speed and direction. It is a fundamental aspect of atmospheric dynamics that significantly affects wind turbine's performance and structural integrity.

Wind turbines operate within the lowest part Atmospheric Boundary Layer (ABL). The ABL is a turbulent layer that extends approximately 1-2 kilometers from the Earth's surface during the daytime (Panofsky & Dutton, 1984). It is the region where the atmosphere interacts with the Earth's surface, resulting in the vertical exchange of momentum, heat, and moisture. This exchange occurs on relatively short timescales, typically within an hour or less (Stull, 1988). The sharpest gradients of the mean wind speed, wind direction, and temperature change occur in the lowest 10% of the ABL which refers to Atmospheric Surface Layer (ASL) (Kaimal & Finnigan, 1994).

During the nighttime, when winds are weak, the thickness of the turbulent layer in the ABL can be significantly smaller, less than 100 meters. However, on windy days or nights, particularly in the presence of thick clouds, the entire ABL becomes fully turbulent, and its depth is determined by wind speed and surface roughness (Panofsky & Dutton, 1984). To model turbulence in the atmospheric boundary layer, it is commonly assumed to be a stationary, ergotic, Gaussian-distributed, and homogeneous random process.

- Random process is an ensemble of random variables that are a function of time (Etienne Cheynet, 2022).

- Stationary random process is stationary if its statistical properties do not change with time (Panofsky & Dutton, 1984). According to Panofsky &

Dutton (1984), stationarity in the atmosphere close to the ground is generally not fulfilled due to regular diurnal changes. Factors such as mean wind speed, mean temperature, and variance of these exhibit variations throughout the day, with an increase from morning to early afternoon followed by a decrease. Weather patterns also contribute to changes, ranging from calm to stormy and cold to warm periods, each associated with distinct small-scale motion statistics. Despite these challenges, selecting specific periods where stationarity is a reasonable assumption is possible. For instance, extended periods of strong winds with thick clouds can minimize day-to-night differences. Additionally, when considering shorter time intervals, such as 10 minutes to one hour, the wind speed is assumed to be a stationary process.

- Ergotic random process implies that statistical properties can be approximated from a sufficiently long single time series (Etienne Cheynet, 2022). In an ideal scenario, turbulent flow properties are described through ensemble averaging, but in reality, time averaging relies upon, the assumption that it is equivalent to ensemble averaging (Kaimal & Finnigan, 1994).

- Gaussian distribution is a probability distribution that exhibits symmetry around its mean value. In this distribution, data points near the mean are more likely to occur compared to those further away from the mean. This means that the majority of the data fall close to the mean, with fewer data points in the tails of the distribution. The shape of the Gaussian distribution is often described as a symmetric bell curve, with the peak representing the mean and the standard deviation determining the spread or width of the distribution. The Gaussian distribution is not a perfect representation of the probabilistic structure of turbulence (Panofsky & Dutton, 1984). However, Gaussian distributions can still be useful for approximations and serve as starting point in studying and analyzing turbulence.

- Homogeneous random process: A random process is homogeneous if its statistical properties do not vary in space (Panofsky & Dutton, 1984).

  According to Panofsky & Dutton (1984), homogeneous flow assumes that statistical properties, such as wind speed and temperature, remain constant and consistent in space. However, achieving true homogeneity in the atmosphere is challenging due to various factors. The presence of the Earth's surface introduces spatial variations in flow statistics, making it difficult to achieve homogeneity except in the horizontal direction.

The distance from the boundary layer affects the statistics, and the flow near the ground is influenced by the local terrain, including hills, valleys, forests, fields, and buildings. While over flat and homogeneous terrain or the ocean, small-scale flows may exhibit some level of horizontal homogeneity, this approximation is generally not valid over most continental areas. Vertical homogeneity is rarely valid near the ground as the mean wind speed and temperature change rapidly with height.

These assumptions allow engineers to analyze and predict the behavior of wind turbines in turbulent wind conditions, taking into account the statistical properties and characteristics of turbulence within the atmospheric boundary layer.

2.1 Turbulence as random process

The statistical description of the wind velocity is described as a three-dimensional stationary random process. For the horizontal mean flow the along-wind (x-axis), the crosswind (y-axis), and the vertical (positive z-axis) wind components are denoted u, v, and w, respectively. The projection of the wind velocity vector within the scanning beam of the lidar system is represented by v_r, also known as radial velocity. For a given height, each velocity component is expressed as the sum of a mean part (temporal average), represented by $\overline{u}$, $\overline{v}$, $\overline{w}$ and $\overline{v_r}$ and a fluctuating part denoted as u', v', w' and v_r'.

$$u = \overline{u} + u' \tag{2.1}$$
$$v = \overline{v} + v' \tag{2.2}$$
$$w = \overline{w} + w' \tag{2.3}$$
$$v_r = \overline{v_r} + v_r' \tag{2.4}$$

In many cases, the mean wind speed is calculated by averaging 10-minute blocks of sampled data obtained from point measurements and is recommended by Commission et al. (2005) and STN (1991). However, it is important to consider the choice of the averaging period, as noted by Panofsky & Dutton (1984); Larsén & Mann (2006), as this can have a significant impact on the estimation of wind statistics. Additionally, Panofsky & Dutton (1984); Wang et al. (2016) has demonstrated that an increasing averaging time results in a greater number of non-stationary wind records.

In the context of a horizontal and stationary flow, when the coordinate system is aligned with the actual mean wind direction $\overline{u} = \overline{u}$ and $\overline{v} = \overline{w} \approx 0$

$m{\cdot}s^{-1}$ (Teunissen, 1980). Over slightly hilly terrain, the wind flow is no longer only horizontal, and $\overline{w} \neq 0$. In the absence of flow separation, flow characteristics can be analyzed using the mean streamlined coordinate system, where $w = 0$. The new coordinate system is obtained by rotating the original coordinate system to align with the mean direction of the streamlines (Wilczak et al., 2001).

The along-beam mean velocity component $\overline{v_r}$ is equal to zero only when the scanning beam is perpendicular to the mean wind flow. The expression for along-beam wind velocity component, v_r 2.4, is given by:

$$v_r = -u\cos(\phi-\theta)\cos(\psi-\alpha) - v\sin(\phi-\theta)\cos(\psi-\alpha) - w\sin(\psi-\alpha) \tag{2.5}$$

where ϕ is the azimuth angle, θ is wind direction, ψ is the elevation angle and α is the angle of attack.

An alternative description to study three-dimensional turbulence was suggested by Taylor (1938). Taylor's frozen turbulence hypothesis states that in a turbulent flow, the small-scale eddies that form the turbulence are frozen into the larger-scale motion of the flow. Following this approach, the wind velocity is measured at a single spatial location over a specific time duration and then transformed into spatial measurements to approximate the turbulence characteristics in the desired area (Stull, 1988). The equation that captures this behavior in turbulence measurements, as described by Tong (1996), is as follows:

$$s'(x,t) = s(x-Ut) \tag{2.6}$$

where the (s') represents the measured flow variable at a fixed spatial point x to the same variable s at a location $x - Ut$, where U denotes the mean convection velocity Tong (1996).

2.1.1 Integral characteristics

Integral turbulence characteristics provide insights into the cumulative effects of turbulence over a specific time or spatial domain. The Reynolds stress tensor quantifies the correlations between velocity fluctuations at different points in space. The variance and covariance of velocity fluctuations, known as Reynolds stresses, are commonly represented by the symmetric Reynolds stress tensor 2.7.

$$R = \begin{bmatrix} \overline{u'u'} & \overline{u'v'} & \overline{u'w'} \\ \overline{u'v'} & \overline{v'v'} & \overline{v'w'} \\ \overline{u'w'} & \overline{v'w'} & \overline{w'w'} \end{bmatrix} \tag{2.7}$$

Where the diagonal terms in 2.7 represent the variances of velocity fluctuations, while the off-diagonal terms represent the covariances between different velocity components.

In the context of steady flow over flat and homogeneous terrain, it is commonly assumed that the Reynolds stress tensor's off-diagonal terms are negligible, except for the $\overline{u'w'}$ term. However, the term $\overline{v'w'}$ is not always negligible in flow over hills or in complex terrain (Midjiyawa et al., 2021b; Zeman & Jensen, 1987). Furthermore, the term $\overline{v'w'}$ can not be disregarded in 10% of ASL within offshore environments (Midjiyawa et al., 2021b).

This finding suggests that the interaction between the vertical and lateral turbulent fluctuations is significant and should be taken into account in some instances. Therefore, in the presence of an escarpment close to the offshore environment as in this study, the term $\overline{v'w'}$ should be taken into account because these obstacles can contribute to additional shear stress.

The surface friction velocity is a fundamental scaling velocity parameter in the study of turbulent flow, particularly in ABL flows Kaimal & Finnigan (1994). Estimating friction velocity in a complex terrain may be a challenging task. However according to Weber (1999) using the horizontal Reynolds stress vector and applying a double coordinate system rotation technique, the friction velocity can be expressed as:

$$u_* = \sqrt[4]{\overline{(u'w')}^2 + \overline{(v'w')}^2} \tag{2.8}$$

The covariance $(u'w')$ represents the kinematic flux of u-momentum in the vertical direction similarly $(v'w')$ represents the kinematic flux of v-momentum flux in the vertical direction Stull (1988). When whole term $\overline{(u'w')}$ or $\overline{(v'w')}$ is considered it quantifies the covariance between the respective velocity fluctuations, capturing the turbulent momentum exchange in the flow McMillen (1988).

In wind engineering, turbulence intensity is crucial for wind fluctuation analysis. Turbulence intensity quantifies the magnitude of velocity fluctuations in a turbulent flow relative to the mean wind speed. The turbulence level can be characterized by the standard deviation of the wind speed, denoted σ. Traditionally, and partly due to the limitation of available measurements, the

wind energy community has primarily focused on analyzing fluctuations in the mean along-wind direction $\overline{u}$ (Stickland, 2012). The associated turbulence intensity for each wind component is defined as:

$$TI_u = \frac{\sigma_u}{\overline{u}} \tag{2.9}$$

$$TI_v = \frac{\sigma_v}{\overline{u}} \tag{2.10}$$

$$TI_w = \frac{\sigma_w}{\overline{u}} \tag{2.11}$$

The σ_u, σ_v and σ_w represents the standard deviation of the u, v, w wind speed components,respectively. The standard deviation of each wind component can be obtained by integrating the corresponding power spectra density estimate $S_i(f)$ over a frequency range using the equation:

$$\sigma_i = \sqrt{\int_0^\infty S_i(f)df} \tag{2.12}$$

Where $S_i(f)$ represents the power spectra density estimate for wind component i, where $i = \{u, v, w\}$. The numerical value of σ is influenced by the duration of the record considered. The wind industry Stickland (2012) relies on 10-minute records. In cases where longer records, such as one hour, the computed value of σ tends to increase due to significant energy at low frequencies in wind spectra.

In addition to calculating the standard deviations of wind speed components, another approach that has gained attention in wind analysis is the use of similarity functions. Originally developed to describe atmospheric stability relationships, this thesis, however, does not primarily focus on atmospheric stability. Instead, the main goal is to validate coherence by comparing lidar and sonic measurements. In this regard, similarity functions will be employed as universal ratios to check whether the sonic data are reasonable. Moreover, the values obtained in this study will be compared with those from studies conducted on flat, homogeneous, and complex terrain.

ϕ_i, ϕ_{vu} and ϕ_{vu} is presumed to represent a set of universal ratios where $i = \{u, v, w\}$.

$$\phi_i = \frac{\sigma_\alpha}{u_*}, \quad \alpha = u, v, w \tag{2.13}$$

$$\phi_{vu} = \frac{\sigma_v}{\sigma_u} \tag{2.14}$$

$$\phi_{wu} = \frac{\sigma_w}{\sigma_u} \tag{2.15}$$

Note that only the equation 2.15 satisfies the Monin-Obukhov similarity theory (Monin & Obukhov, 1954).

These universal ratios 2.13, which are normalized by the scaling parameter friction velocity (u_*) describe a measure of the variability of the wind speed in the streamwise, crosswise, and vertical directions. The ratios 2.14 and 2.15 offer insights into the directional characteristics of wind turbulence. A value of ϕ_{vu} or ϕ_{wu} greater than one indicates that the crosswind or vertical component, respectively, is more variable compared to the streamwise component. Conversely, if the values are less than one, it suggests that the streamwise component is more dominant and the wind exhibits less variability in the crosswind or vertical direction, respectively.

2.1.2 The power spectral densities

The power spectral density (PSD) of the wind fluctuations often called wind spectrum, describes how the power of the wind turbulence is distributed over the frequencies. The wind spectrum can be divided into three distinct frequency ranges low, medium, and high.

In the low-frequency range, large-scale eddies are generated, and the slope of the PSD for the low-frequency range is typically close to or slightly above zero. This range is referred to as the production range, as it represents the generation of turbulent energy through processes like convection or vertical shear in the mean flow. This frequency range holds significant relevance for offshore wind turbine response (Nybø et al., 2020).

Medium-frequency range, which is denoted as the inertial subrange, is where the energy obtained from larger eddies is balanced by the energy dissipated into smaller eddies. This range exhibits the characteristic Kolmogorov Kolmogorov (1941) slope of -5/3, representing the scaling behavior of turbulence in the inertial subrange.

The high-frequency range, known as the Kolmogorov dissipation range, is characterized by fast motions and the dissipation of turbulent energy(Kolmogorov, 1941; Kaimal & Finnigan, 1994; LUMLEY & PANOFSKY, 1964).

In addition to the PSD analysis of wind fluctuations, another important aspect of characterizing wind turbulence is the examination of single-point cross-power spectral densities and two-point (CPSD). The Single-point CPSD calculates the cross-correlation between two different signals at one given spatial point while the two-point CPSD calculates the cross-correlation between two signals at different spatial points.

The PSD and CPSD in this thesis are computed by using Welch's algorithm method (Welch, 1967). The application of Welch's algorithm involves dividing

the signal into overlapping segments. Each segment is windowed, using a window function, to reduce spectral leakage. The Fast Fourier Transform (FFT) is then applied to each windowed segment to obtain periodogram estimates. The periodograms from the individual segments are then averaged together, typically using an arithmetic mean, to generate the final estimate of the PSD. Welch's method represents an advancement over the standard periodogram spectrum estimating method by effectively reducing noise in the estimated power spectra. This noise reduction capability, however, comes at the cost of a reduction in frequency resolution. However, considering the presence of noise in wind measurements, which can arise from various sources such as measurement errors, environmental conditions, and inherent variability, the noise reduction provided by Welch's method is often desirable.

In addition to analyzing the PSD of wind fluctuations, it is important to examine the ratios of normalized power spectral densities in the inertial subrange. This subrange, characterized by the balancing of energy between larger and smaller eddies, exhibits distinct spectral behaviors. In the inertial subrange, Kaimal et al. (1972); Kolmogorov (1941) established an asymptotic relation for the normalized power spectra densities of three wind velocity components. Their findings revealed that spectral levels in the lateral and vertical directions are higher than those in the longitudinal direction by a factor of 4/3, as predicted by isotropy. The relationship is generally observed in flat and homogeneous terrain for all but most of the neutral atmospheric conditions (Kaimal et al., 1972). In the regime where the inertial subrange, where the frequency f_r is much greater than 1, the ratios of the normalized power spectral densities can be approximated as follows:

$$\frac{S_w}{S_u} \cong \frac{S_v}{S_u} \approx \frac{4}{3}, \quad at \;\; f_r >> 1 \tag{2.16}$$

Statistical isotropy of the second order implies that the second-order statistics remain unchanged when the coordinate system is rotated in any direction. This would result in identical variances for the three velocity components and zero covariances (Peña et al., 2019). In the context of turbulence, isotropy implies that statistical properties, such as velocity fluctuations or energy transfers, are independent of the direction in which they are measured. Even though isotropy does not apply to the production frequency range of turbulence, we may assume that the small-scale structures are effectively isotropic (Kaimal & Finnigan, 1994). This assumption of local isotropy is crucial for deriving small-scale turbulence statistics. It suggests that within that particular range, the statistical properties exhibit isotropic behavior.

2.1.3 Modeling the wind velocity spectrum

In the field of wind engineering, the velocity spectrum S_u, S_v, and S_w is often modeled considering an empirical relationship. These models aim to capture statistical characteristics of wind velocity fluctuations and are crucial for designing structures and assessing their response to wind loads. The most commonly used model in wind engineering for the along-wind velocity spectrum is known as the "blunt model" (Olesen et al., 1984; Tieleman, 1995). This model is based on the broader and less sharp spectral peak, which captures the dominant frequency within wind velocity spectra.

The "pointed model" is the traditional choice for representing the vertical velocity spectrum, known for its characteristic of a sharper spectral peak (Olesen et al., 1984; Tieleman, 1995).

In this thesis, wind spectrum analysis is presented from measured sonic anemometer data and by using spectral models proposed by Kaimal et al. (1972). The Kaimal spectrum, derived from the research conducted by Kaimal et al. (1972), provides an empirical representation of the power spectral densities of wind velocity components in the neutral atmospheric boundary layer. Spectral models for lateral separation and cross-section, which are based on the blunt model, are expressed as follows:

$$\frac{fS_u}{{u_*}^2} = \frac{105 f_r}{(1+33f_r)^{5/3}} \tag{2.17}$$

$$\frac{fS_v}{{u_*}^2} = \frac{17 f_r}{(1+9.5f_r)^{5/3}} \tag{2.18}$$

$$\frac{fRe(S_{uw})}{{u_*}^2} = \frac{14 f_r}{1+9.6f_r^{7/3}} \tag{2.19}$$

Where $Re(S_{uw})$ represents the real part of cross-spectral density between the along-beam u and vertical w wind velocity components; f is a frequency and f_r is the reduced frequency defined as:

$$f_r = \frac{fz}{\overline{u}(z)} \tag{2.20}$$

Where $\overline{u}$ is the mean wind speed and z is the altitude from the surface to a reference point. The vertical velocity component, which follows the pointed model, is expressed as:

$$\frac{fS_w}{{u_*}^2} = \frac{2 f_r}{1+5.3f_r^{5/3}} \tag{2.21}$$

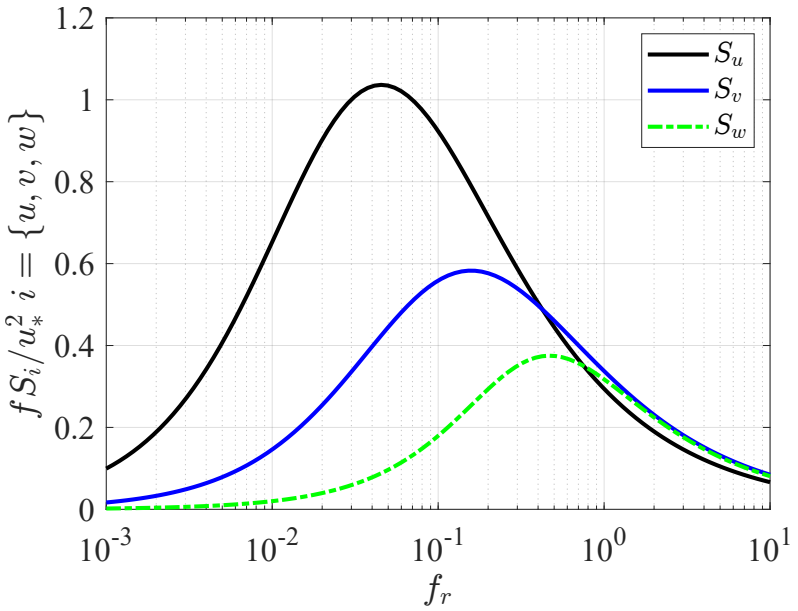

Figure 2.1: Kaimal empirical normalized spectral models for along-wind (S_u) and cross-wind (S_v) components based on the Blunt Model (Solid lines) and for vertical wind direction (S_w) based on the pointed model (Dashed line).

2.1.4 Atmospheric stability

The thermal stratification of the atmosphere has a connection to turbulence characteristics measurements in the ABL. Static stability and dynamic stability are two distinct concepts used to analyze atmospheric conditions.

Static stability depends on the resistance of air parcels against vertical displacement, determined by the temperature distribution in ABL. If the temperature decreases more rapidly with height than the adiabatic lapse rate (the rate at which a parcel of air cools as it rises or warms as it descends), the atmosphere is considered statically stable. Conversely, if the temperature decreases at a slower rate, it is statically unstable. Dynamic stability, on the other hand, pertains to the ability of the atmosphere to dampen or amplify disturbances over time. It accounts for the interaction between the motion of the air parcels and the larger-scale atmospheric flow. Dynamic stability is influenced by factors such as wind shear, vertical wind speed variations, and the presence of atmospheric waves.

In this study, there was a desire to obtain dynamic stability measurements using a 3D sonic anemometer and to have the opportunity to apply the Monin-Obukhov similarity theory length to determine atmospheric stability. However, the sonic anemometers deployed at the end of the COTUR campaign did not store the sonic temperature. As a result, it was not possible to estimate the

dynamic stability of the atmosphere using the data from the sonic anemometers. Therefore this study chooses not to include the study of atmospheric stability. It is worth noting that during the COTUR measurement campaign, the majority of high-quality data was associated with either unstable or near-neutral atmospheric conditions Cheynet et al. (2021).

2.2 Coherence analysis in wind engineering field

The coherence of turbulence analysis takes a significant part in the field of wind engineering. Coherence is crucial for understanding the spatial correlation of turbulence and its implications for estimating wind loads on structures, such as wind turbines, long-span bridges, and high-rise buildings (Doubrawa et al., 2019; Miyata et al., 2002; Macdonald, 2003; Bietry et al., 1995).

The spatial correlation of eddies must be analyzed in terms of vertical and lateral coherence for wind turbine design. In this context, lateral coherence indicates the coherence of one of the wind velocity components within the horizontal plane specifically in crosswind direction (Cheynet et al., 2021). Vertical separations are described as vertical coherence.

Coherence between two points in the atmosphere is defined as the normalized cross-spectrum between the time series of turbulent wind velocities at these two points. The coherence can vary between one and zero, where a significant value indicates high correlations between two spatially separated points at the same frequency. Coherence intensity is dependent on mean wind speed, frequency, atmospheric stability, height, velocity component, and separation distance (Brook, 1975; Soucy et al., 1982; Cheynet et al., 2018b) The coherence is a decreasing function of separation distance and frequency. As the separation distance between two spatial measured points increases, coherence tends to decrease. Similarly, coherence decreases exponentially with higher frequencies. Coherence tends to increase with higher mean wind speed and decreasing atmospheric stability. Whereas higher mean wind speed generally leads to more organized and coherent wind flow. Resulting that fluctuations in wind speed at one location are more likely to be reflected at another location.

The most straightforward approach to studying the horizontal coherence of turbulence is to use at least two anemometers, at the same measurement height, located along a line perpendicular to the wind direction. Davenport (1961); Pielke & Panofsky (1970); Ropelewski et al. (1973) One of the first coherence characterization studies for lateral separations was made by Ropelewski et al. (1973) back in 1972. Where the coherence for stream-wise and cross-stream wind components was studied. In their study, coherence was

investigated using an array of met-mast to capture time series of turbulent wind velocities. However, the deployment of met-masts in complex terrain or offshore environment can be challenging and costly Midjiyawa et al. (2021a,b). More recently, remote sensing technologies such as lidars have been employed for coherence analysis. Lidars use laser beams to measure wind characteristics at multiple points in space, allowing for a more comprehensive assessment of coherence over larger areas (Cheynet et al., 2016).

The square-root of the coherence is called the root-coherence and is a complex function. The real part is called the co-coherence and the imaginary part is called the quadrature spectrum (quad-coherence). Where co-coherence describes the correlation between two variables at spatially separated points. While quad-coherence focuses on the phase or timing, quantifying the degree of synchronization of these variables. The root-coherence (γ_{ij}) between two velocity components i and j, where $i, j = u, v, w$ and between two points in space (x_1, y_1, z_1) and (x_2, y_2, z_2). is given by

$$\gamma_{ij}(f, x_1, y_1, z_1, x_2, y_2, z_2) = \frac{S_{ij}(f, x_1, y_1, z_1, x_2, y_2, z_2)}{\sqrt{S_i(f, x_1, y_1, z_1) S_j(f, x_2, y_2, z_2)}} \tag{2.22}$$

Where $S_{ij}(f, x_1, y_1, z_1, x_2, y_2, z_2)$ is the two-point cross-spectral density between the i and j velocity compoenets. $S_i(f, x_1, y_1, z_1)$ and $S_j(f, x_2, y_2, z_2)$ are the one-pint spectra estimated at coordinates (x_1, y_1, z_1) and (x_2, y_2, z_2). For two points located on a horizontal line perpendicular to the wind direction at coordinates y_1 and y_2, the co-coherence γ_{ij}, where $i = u, v, w$ is defined as

$$\gamma_{ij}(y_1, y_2, f) = \frac{Re\{S_{ij}(y_1, y_2, f)\}}{\sqrt{S_i(y_1, f) S_i(y_2, f)}} \tag{2.23}$$

where $S_i(y_1, y_2, f)$ is the two-point cross-spectral density of the i and j components between two spatial points y_1 and y_2; $S_i(y_1, f)$ and $S_i(y_2, f)$ is a single point spectrum of the i component measured at two spatial point y_1 and y_2, respectively. In wind engineering, the assumption is commonly made that root-coherence is equivalent to co-coherence, leading to the neglect of the imaginary part of root-coherence. This is due to the observation that the imaginary component tends to have relatively less significant when compared to the co-coherence (Frost et al., 1978). Veers (1984) suggested that under certain assumptions, such as assuming perfect phase alignment in wind velocity fluctuations, quad-coherence could be ignored without significantly affecting the accuracy of the analysis.

Concerning the estimation of coherence in the field of wind engineering, several empirical models have witnessed the development of empirical coherence estimation (Solari & Piccardo, 2001). One of the first empirical

models developed by Davenport (1961) describing vertical co-coherence is the Davenport coherence model. Which for $i = \{u, v, w\}$ is given by

$$\gamma_i(z_1, z_2, f) = \exp\left(-\frac{c_z^i f \delta_z}{\overline{U}(z_1, z_2}\right) \tag{2.24}$$

where c_z^i is a constant called exponential decay its determination relies on experimental methods; $\delta_z = |z_1 - z_2|$ is two measurements at heights z_1 and z_2; $\overline{U}$ is average mean wind speed between heights z_1 and z_2, mathematically explained as:

$$\overline{U}(z_1, z_2) = \frac{1}{2}\left[\overline{u}(z_1) + \overline{u}(z_2)\right] \tag{2.25}$$

The Davenport model initially design for vertical separations, was later generalized and applied for lateral and longitudinal separations (Pielke & Panofsky, 1970; Ropelewski et al., 1973). The Davenport model finds extensive application in wind engineering due to its simplicity and effectiveness in assessing the coherence of turbulence at relatively small separation, typically below 50 meters (Kristensen & Jensen, 1979).

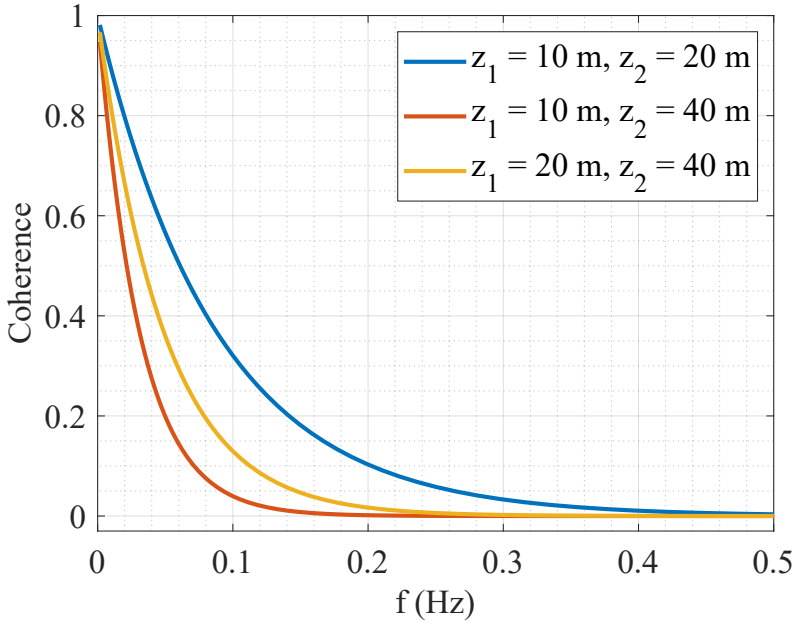

Figure 2.2: An example of Davenport vertical coherence model for different height separations using a decay parameter c_u = 7.

2.3 Sonic anemometer technology

The sonic anemometer was developed in the 1950s and is also known as an ultrasonic anemometer (Klein, 1948). The sonic anemometer is a device used to measure instantaneous wind velocity and direction. It works by emitting high-frequency sound waves and measuring the time it takes for the sound to travel between a pair of transducers. By measuring the speed of sound in the air, which can be accelerated or decelerated by the effect of the wind, the anemometer can calculate wind velocity(Axaopoulos & Tzanes, 2022).

The sonic anemometer is very accurate and precise, it is able to measure wind velocity with an accuracy of 0.1 $m{\cdot}s^{-1}$ (Axaopoulos & Tzanes, 2022). In addition to wind measurements, the sonic anemometer can measure so-called sonic temperature by using the speed of sound which depends on temperature and humidity.

The anemometer typically consists of two or three ultrasonic transducers, each of which emits and receives sound waves. The transducers are mounted on a mast or boom and are oriented at different angles to measure wind velocity and direction.

Sonic anemometers are commonly used in applications such as meteorology, wind energy, ship navigation, aviation, and other fields where wind speed and direction need to be measured. The absence of moving parts is a significant advantage of sonic anemometers, making them highly suitable for long-term deployment in exposed automated weather stations and weather buoys. Unlike traditional cup-and-vane anemometers, which can be negatively impacted by factors such as salty air or excessive dust, sonic anemometers maintain their accuracy and reliability in such challenging environments (Axaopoulos & Tzanes, 2022). Sonic anemometers are also popular in many meteorological applications, such as weather forecasting, climate research, and air pollution measurements, as they provide high-resolution data that can be used to study the dynamics of the atmosphere.

2.4 Scanning Lidar technology

Lidar is an acronym for light detection and ranging. It is a remote sensing technology that measures wind speed and direction. The lidar system uses light in the form of an emitted laser beam to the atmosphere to determine the movement of particles known as aerosol (Peña et al., 2013). Lidar systems measure the frequency shift in the backscattered beam resulting from the interaction between the emitted laser beam and aerosol particles in the atmosphere. This frequency shift is used to determine wind velocity along the beam, assuming

a homogeneous wind flow for combining radial measurements into a single wind vector (Peña et al., 2013).

Wind lidar systems made their first debut in the 1970s, and have since been applied in various fields, including wind energy, aviation, and meteorology (Jelalian, 1992). However, early wind energy applications in the 1980s were hindered by the high cost and large size of lidar systems at that time (Hardesty & Weber, 1987; Vaughan & Forrester, 1989). In the 2010s, wind lidar technology gained significant traction, especially for wind resource assessment (Peña et al., 2013).

Lidar systems can be categorized into two main groups coherent Doppler lidar and direct-detection Doppler lidar (Werner, 2005). Coherent lidar systems utilize the process of light beating to measure the Doppler shifts in the frequency of backscattered light (Slinger & Harris, 2012). This is achieved by comparing the frequency shift of the laser beam as it interacts with aerosol particles to that of a reference beam (Chanin et al., 1989). While direct detection lidar as explained by Chanin et al. (1989); Rodrigo & Pedersen (2015) utilize an optical filter, such as a Fabry-Perot etalon, to measure frequency shifts. The collected backscattered light is passed through the filter, allowing only specific frequencies to pass through, which enables the system to detect intensity changes associated with the desired target properties.

Coherent lidar systems are classified into three key parameters. According to Slinger & Harris (2012), these parameters include the emission waveform (pulsed or continuous), waveband (visible, near-IR, far-IR), and the transmit/receive geometry (monostatic or bistatic). In the COTUR campaign, two types of Lidar systems were used Doppler wind profiler Leosphere WindCube V1 and Scanning Doppler wind lidar Leosphere WindCube 100S. They refer to pulsed wave coherent monostatic lidar systems that operate in near-infra-red (near-IR) band 1.54 μm (Pauliac, 2009). The following information about lidar will focus on systems types utilized in the COTUR campaign.

Doppler wind profiler Leosphere WindCube V1 is a land-based lidar system that measures the vertical radial wind velocity simultaneously in multiple directions above its position. A Doppler wind profiler lidar is based on a Doppler beam swinging (DBS) scanning pattern by emitting a sequence of pulsed beams in three or more inclined directions (Peña et al., 2013). A Doppler wind profiler lidar uses the DBS scanning pattern to gather more information along the line of sight (LOS) by averaging multiple measurements.

(LOS) refers to the direction along which the coherent lidar system measures the wind. The beam direction is adjusted by rotating mirrors or wedge prisms by angles of 90 ° or 120° (Werner, 2005). The specific angle depends on the number of measurement beams and follows a conical scan pattern. The

cone angle in vertical Doppler profiler systems represents a balance between velocity resolution and atmospheric stability. A smaller cone angle results in better wind homogeneity but may lead to a less accurate projection of the wind vector on each beam. Research by Boquet et al. (2010) has shown that optimal values for cone angles are between 15° and 30°.

The reconstruction of the 3D wind vector can be achieved by using three or four radial velocities at each measurement height. When using three beams, the solution for the wind vector is unique. If one of the three axes is accurately aligned with the vertical direction, it enables the accurate determination of the vertical component (Werner, 2005). On the other hand, with four beams, the additional equation enables the assessment of wind homogeneity and helps avoid undesired values (Peña et al., 2013).

The Scanning Doppler wind lidar Leosphere WindCube 100S uses the same Doppler shift technology as the Doppler wind profiler Leosphere WindCube V1. However, the key difference lies in the capabilities of the Scanning Doppler wind lidar to measure the along-beam wind velocity component at greater distances from the observer.

Unlike the Doppler wind profiler which focuses on vertical profiling of the wind, the Scanning Doppler wind lidar is designed to measure the wind velocity component along the scanning beam. This allows for measurements to be taken simultaneously at multiple positions along the beam, covering distances of several kilometers from the observer.

Scanning pulsed Doppler wind lidars are equipped with a scanner head capable of adjusting the orientation of the scanning beam. The scanner head has a rotational range of 0 ° to 360° in azimuth angle and -10° to 190° in elevation angle (2.3).

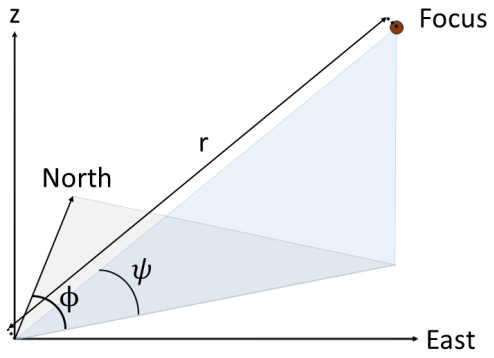

Figure 2.3: Azimuth angle ϕ, elevation angle ψ, and radial distance r defined for a scanning wind lidar. The sketch is inspired by Cheynet (2016).

Scanning lidar also uses the Doppler principle to measure the Line-Of-Sight (LOS) wind speed. When the received wave is compressed, it indicates that the wind is moving toward the lidar. Conversely, if there is an expansion of the wave at the receiver, it implies that particles are moving away from the lidar. When the backscattered beam has the same frequency as the transmitted beam, it indicates either no wind or wind coming perpendicular to the lidar's measurement direction. This frequency shift denoted as f_s can be expressed by the following equation

$$f_s = \frac{2V_{LOS}}{\lambda} \tag{2.26}$$

where V_{LOS} is aerosol speed along the line of sight velocity and λ is the wavelength of the emitted pulse light approximately 1.54 μm. With the assumption that aerosols are moving ideally with the wind, V_{LOS} can be determined by

$$V_{LOS} = \left| (u + v + w) \cdot \frac{x + y + z}{\sqrt{x^2 + y^2 + z^2}} \right| \tag{2.27}$$

where $\{x + y + z\}$ is a specific measurement location.

For accurate LOS measurements, it is important to consider the Carrier-to-Noise Ratio (CNR). The CNR reflects the ratio of the signal backscattered to the lidar's receiver compared to the signal emitted into the atmosphere (Werner, 2005). In situations where there is a minimal amount of aerosols present, the

CNR value tends to be low. This means that in clear atmospheric conditions, the lidar may struggle to accurately measure wind speed and direction. In general, a CNR value lower than -28dB is considered indicative of a weak signal, resulting in lower-quality data.

2.4.1 The Spatial Averaging effect

A Doppler scanning wind Lidar measures the wind velocity within a volume along the scanning beam. The resulting velocity along the beam represents a low-pass filtered version of the actual wind velocity at each measured point in the volume (Cheynet et al., 2017b). Modeling the spatial averaging effect is essential to accurately assess the impact to which the instrument's performance impacts wind turbulence measurements. This involves estimating the measurement bias in the standard deviation of wind velocity and determining the wind velocity spectrum frequency above which the along-beam spatial averaging becomes negligible (Cheynet et al., 2017b).

The scanning Lidar measurement can be expressed as a scalar convolution of the spatial averaging function ϕ and the vector of the wind velocity $\mathbf{v}$, at a focus position $\mathbf{r}$ (Smalikho, 1995). The along-beam wind velocity can be expressed by integration along the laser beam of the unit vector $\mathbf{n}$ and the distance from the focus point along the beam $\mathbf{s}$.

$$v_r(r) = \int_{-\infty}^{\infty} \phi(s)\mathbf{n} \cdot \mathbf{v}(s+r)\mathbf{n}ds \tag{2.28}$$

When the beam from the scanner is pointing in the same direction as the wind, then it is possible to calculate the equation 2.28 by using a scalar convolution product. For a scanning wind lidar, the weighting function ϕ is normalized to unit integral and therefore can be written as (Mann et al., 2009):

$$\phi(s) = \begin{cases} \dfrac{l-|s|}{l^2} & \text{if } |s| < l \\ 0 & \text{otherwise} \end{cases} \tag{2.29}$$

where l is the probe length size which refers to the length of the laser pulse that is emitted, i.e., the range within which the lidar signals are measured. The spectral transfer function H corresponding to the spatial averaging function is:

$$H(k) = \left(\frac{\sin(\frac{kl}{2})}{\frac{kl}{2}} \right)^2 \tag{2.30}$$

where k is the wavelength, which is expressed as:

$$k = \frac{2\pi f}{\overline{u}} \tag{2.31}$$

where f is wave frequency and $\overline{u}$ is the mean along-wind velocity component through which the wave is propagating. The standard deviation of the along-wind component σ_u can be calculated by incorporating the spectral transfer function $H(f)$ if the beam is perfectly parallel to the mean wind direction. This calculation yields an expression for the standard deviation that is formulated as a function of the spectral transfer function.

$$\sigma_u = \sqrt{\int_0^\infty H^2(f) S_u(f) df} \tag{2.32}$$

where $Su(f)$ is the power spectral density of the along-wind component velocity fluctuations. The single-point standard deviation of the along-wind component if there is no along beam spatial averaging affect $\sigma_{u_{ref}}$ is then:

$$\sigma_{u_{ref}} = \sqrt{\int_0^\infty S_u(f) df} \tag{2.33}$$

The relative error in σ_u denoted as ϵ:

$$\epsilon = \frac{\sigma_u - \sigma_{u_{ref}}}{\sigma_{u_{ref}}} \tag{2.34}$$

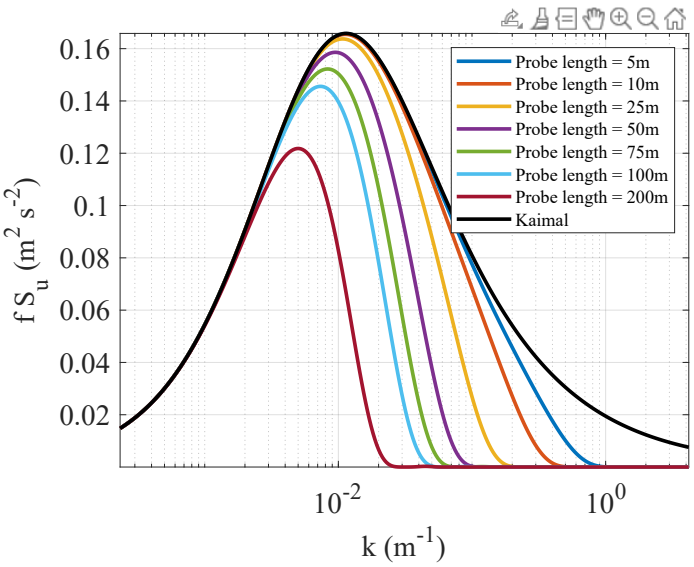

Figure 2.4: Influence of the along-beam spatial averaging affect for different scanning lidar probe lengths for the normalized spectra. Using mean wind velocity $\bar{u} = 15\ m{\cdot}\mathrm{s}^{-1}$ at height z = 25 m.

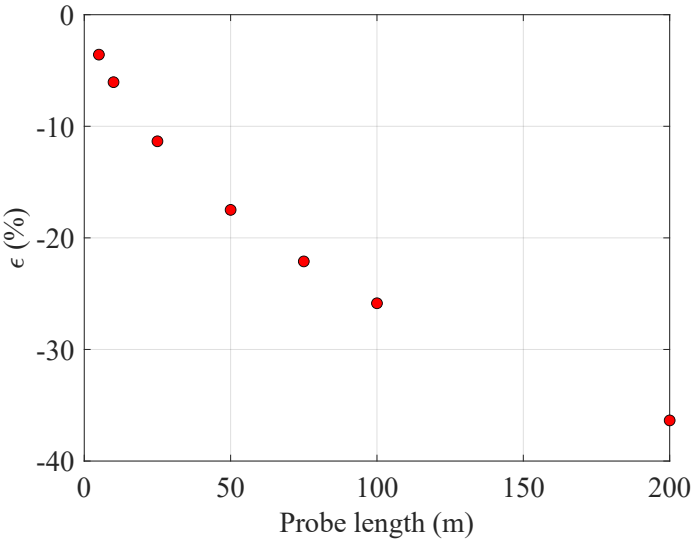

Figure 2.5: Relative error (ϵ) in the standard deviation of the along-wind component caused by the spatial averaging effect for the scanning lidar, as a function of the measured probe length.

Chapter 3

Instrumentation and methods

3.1 Site description

The data evaluated in this study is obtained from long-range scanning lidar and 3D sonic anemometer measurements conducted as part of the COTUR campaign. The COTUR campaign is carried out on the southwestern coast of Norway near the Obrestad lighthouse, spanning from February 2019 to March 2020 (Cheynet et al., 2021). For the purpose of this thesis, only the data collected between March 16, 2020, and March 30, 2020, is utilized.

The site was selected due to its similarity to offshore environments, providing an opportunity to observe relatively undisturbed ocean wind conditions with a large fetch and wide open section (Cheynet et al., 2021). Additionally, the site's accessibility and necessary infrastructure made it well-suited for conducting measurements. The selection of the measurement site was based on several important criteria. The local wind conditions were a priority, with a preference for westerly winds and a large ocean fetch. The site is expected to be open, without mountains near the coast, which could influence the flow field at a mesoscale level.

The Obrestad Lighthouse site is situated on a relatively flat topography that continues up to 10 km inland. The lighthouse and six residential buildings are located on a small flat plateau 25 meters above sea level to the east of an escarpment (Cheynet et al., 2021). The escarpment lies within the level change shown in figure 3.1 with steep slopes of 25-to-35-degree angle which can alter the dynamic and static flow characteristics at a micro-scale level Cheynet et al. (2021). The escarpment at Obrestad Lighthouse has a height twice that of a Bolund hill, which has been extensively studied to enhance the modeling of atmospheric flow in complex terrains(Berg et al., 2011; Bechmann et al., 2011; Lange et al., 2016; Ma & Liu, 2017). Findings from these experiments suggest

that the local flow characteristics at Obrestad Lighthouse could be affected up to 50 m above the instruments due to the presence of the escarpment (Cheynet et al., 2021).

Additionally, the presence of six residential buildings and the Obrestad Lighthouse, with a height of 16.5 meters (Bjørkhaug & Poulsson, 1986), may have an impact on both low and high-frequency fluctuations in their wake. Hertwig et al. (2019) conducted a study on the wake characteristics of tall buildings, revealing that these structures significantly influence the generation of large eddies within the main wake. Moreover, this alteration in the wake structure can be attributed, at least partially, to the influence of smaller-scale and less organized eddies produced by the low-level canopy.

The data collected from the sonic anemometers and wind lidar are divided into five sectors covering different regions to obtain a better understanding of the distribution and behavior of turbulent wind fluctuations across various roughness scales. Table 3.1 presents the sectors that describe different regions and roughness scales based on their orientation relative to the mast positions.

The inland sector is characterized by its flat terrain and relatively uniform surface properties. It has a relatively stable and moderate roughness scale, with regular vegetation cover consisting of grass, larger stones, and bushes, which create a stable and predictable roughness.

The Lighthouse sector can be described as most influenced by the obstacles and infrastructure surrounding it. Structures such as residential buildings and the lighthouse may influence natural wind in the manner of splitting low-frequency fluctuations into high-frequency fluctuations, resulting in increased turbulence intensity.

The escarpment sector with steep slopes and a short distance to the sensors may have an easily detectable higher influence on natural wind flow. As previously discussed, such steep escarpments can affect natural wind up to 50 meters above the ground.

The ocean sector, exposed to the open ocean, is considered smooth. The coastline in this sector is relatively flat, with no significant obstacles that could impact natural wind flow. This terrain type is often associated with low roughness lengths and low surface roughness conditions.

According to the long-term wind observations from a weather station located at Obrestad Lighthouse show that the prevailing wind direction is from the northwest and southeast (Cheynet et al., 2021). Consequently, wind measurements within the 345° to 20° range are much less frequent. In contrast to the other sectors, the wind patterns in the northern sector exhibit less consistency and are influenced by various factors, such as hills and rocks. As a result, the northern sector can be described as a combination or fusion of

the characteristics observed in the inland, ocean, and escarpment sectors.

Table 3.1: Sector classification based on prevailing roughness scales relative to masts orientation.

Sector Name	Wind direction range
Inland sector	120°-180°
Lighthouse sector	180°-210°
Escarpment sector	210°-300°
Ocean sector	300°-330°
Northern sector	330°-20°

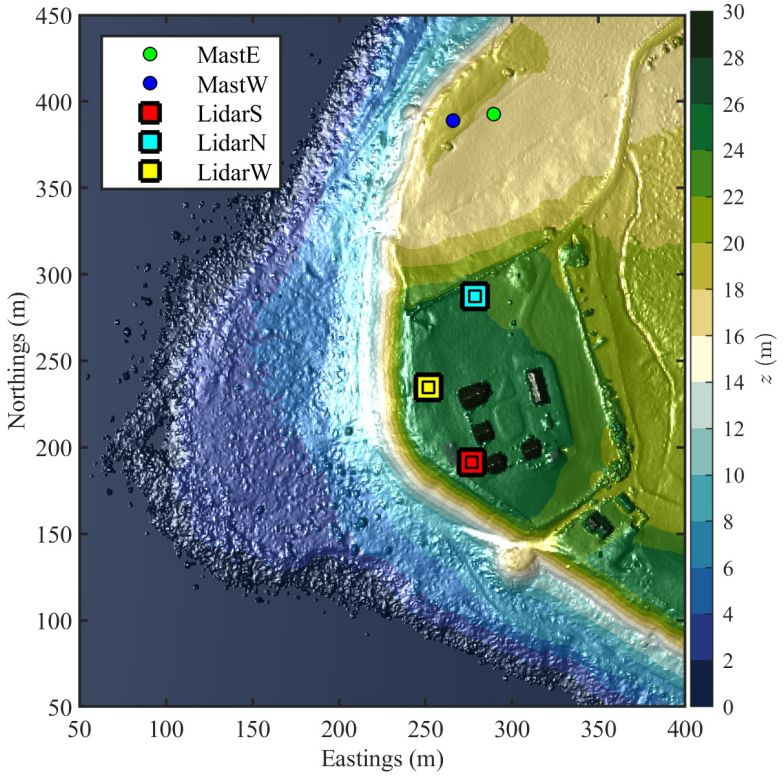

Figure 3.1: Instrumentation positions and local topography at the measurement site. The local topography was obtained from a digital surface model that can represent both natural and artificial features. This model was generated using airborne laser altimetry with a horizontal resolution of 1 meter. Source: (Cheynet et al., 2021).

3.2 Instrumentation

Three long-range wind lidar instruments, specifically the Leosphere WindCube 100S, were deployed near the Obrestad lighthouse from February 2019 to April 2020. However, for this study, data obtained from two of the three lidars will be considered further.

The instruments in the COTUR campaign are named based on the cardinal directions. This study will adopt the same naming convention, as shown in Figure 3.1. Accordingly, LidarN represents the lidar positioned in the north, and LidarW represents the lidar positioned in the west. The Lidar instruments were mounted on a tall platform during the campaign. Specifically, LidarW was positioned 2 meters above the ground, while LidarN was placed 3 meters above the ground to compensate for the slightly lower terrain at its location. Consequently, the scanner heads of two Lidars were approximately 28 meters asl. Wind data collected with the scanning wind lidars were sampled at a frequency of 1 Hz.

Between March 16 and March 30, 2020, as part of the COTUR campaign, two telescopic meteorological masts (PT180-6-NC) from Clark Masts were deployed in an open area. The masts were spaced 20 meters apart from each other and positioned at a distance of approximately 100 meters from LidarN (Cheynet et al., 2021). Each mast was equipped with a 3D sonic anemometer on its top and positioned approximately 11 meters above the ground. As a result measurement volumes of sonic anemometers were, located approximately 28 meters asl.

The sonic anemometers used in this study are Gill WindMaster 3-axis ultrasonic wind sensors. These sensors operate at a high sampling frequency of 20 Hz. The west and east sonic anemometers were located approximately 157 and 169 meters from the lighthouse, respectively. Although each anemometer mast was prepared with a spirit level to guarantee that the anemometers were mounted horizontally, non-zero tilt angles were observed in the anemometer records.

Figure 3.2: WindCube 100S (LidarN) in the center installed 3 m above the ground to compensate for lower terrain at the position WindCubeV1 to the right and Radiometer Physics HATPRO RG4 to the left. Instruments are installed on the Bosch Rexroth aluminum strut profiles. View towards the North direction. Source: (Cheynet et al., 2021)

Figure 3.3: Two telescopic masts equipped with 3D sonic anemometers on their top at a height of 11 m above the ground with a separation distance of 20 m between then and approximately with 100 m distance from the LidarN. Source: (Cheynet et al., 2021)

3.3 Defining Line-Of-Sight strategy

Two pulsed lidar sensors were chosen to operate in staring mode, with each sensor directed towards a sonic anemometer on the mast. To ensure unobstructed measurements and prevent ground-level obstacles from blocking the lidar laser beam, both lidars were mounted on a tall platform. The LOS scanning beams of LidarN and LidarW were orientated towards the sonic anemometers east and west. As shown in figure 3.4, the azimuth angle between LidarW and MastW was 5.3°, with zero elevation angle. Similarly, the azimuth angle between LidarN and MastE was 5.8°, also with zero elevation angle.

The LOS scans were performed using a 25-meter probe volume length with an overlapping of 24 meters. This indicates that there was a 24 meters long region where the probe volumes of adjacent beams were intersected, leading to the creation of a shared area of measurements. This overlapping region ensured that there was sufficient coverage and data continuity between the adjacent beams for accurate wind measurements.

To identify and remove outliers in LOS wind velocity measurements, a common approach involves applying a fixed CNR threshold (Krishnamurthy et al., 2013). Measurements with low CNR values indicate poor quality of LOS velocity. Typical threshold values for CNR in wind measurements range between -23 dB and -27 dB. These thresholds are commonly used to determine the acceptability of the CNR values, with wind data below the threshold being considered unreliable and often discarded as outliers. A CNR threshold for pulsed wind lidar suggested by Pearson et al. (2009) is -23dB while the minimum threshold of -27dB advised by Kumer et al. (2014).

According to Alcayaga (2020); Valldecabres et al. (2018) applying a strict CNR threshold for excluding data points with values below a certain level can result in the removal of an excessive amount of data. This can be a crucial matter when there is a scarcity of data available overall. Therefore it was applied a fusion of two methods without iteration in order to maintain higher data availability. The first method aimed to recover realistic data with a CNR below -27.5 dB. This was accomplished by employing the Mahalanobis distance Mahalanobis (2018), which measures the distance of a data point from the mean value of a distribution in terms of standard deviations. In the COTUR campaign, any data point exceeding a Mahalanobis distance of 20 was regarded as an outlier and subsequently eliminated (Cheynet et al., 2021). The second method applied a CNR threshold where measurements below CNR of -35 dB were automatically discarded (Cheynet et al., 2021).

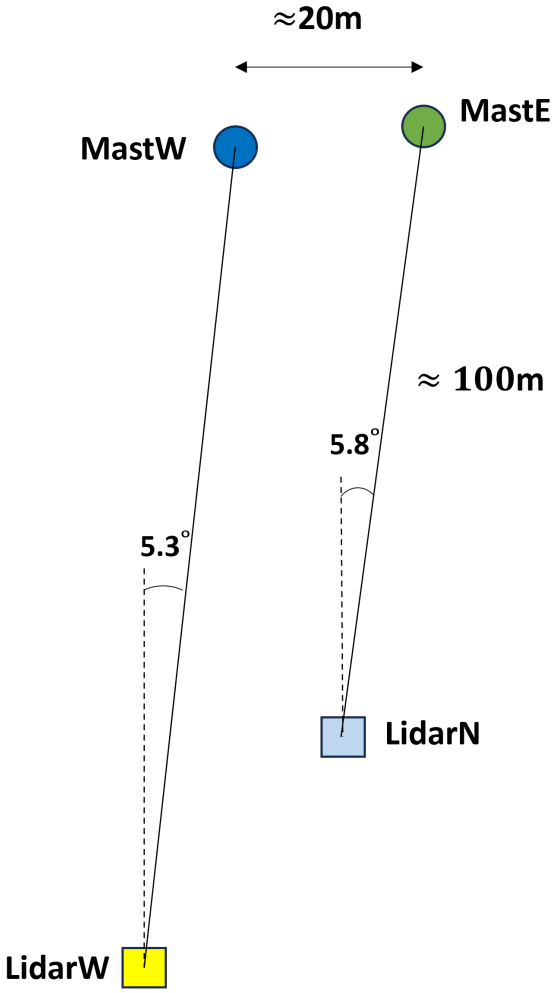

Figure 3.4: Sketch of the scanning strategy and positions of the masts with mounted sonic anemometers with respect to LidarN and LidarW. The lidars operate in Line-Of-Sight staring modes with nearly parallel beams and zero elevation angle. The sketch is inspired by a report by Cheynet (unpublished).

3.4 Data Pocessing

The scanning lidars operated in a LOS scanning mode with a scan duration set to 50 min, however, instrument acquisition errors occasionally resulted in shortened time series (Cheynet et al., 2021). In the field of meteorology, the turbulence characteristics in the ABL are generally analyzed using a time series of 30 minutes or longer (Smith, 1980; Stull, 1988). This is to ensure that a sufficient number of eddies pass through the measuring volume of the

instrument to accurately estimate the wind flow characteristics (Kaimal & Finnigan, 1994). Accordingly, the LOS scan scenarios with a duration shorter than 30 minutes were excluded.

In the wind engineering field, the time-series duration generally ranges between 10 min and 60 min (Kareem & Tamura, 2013). This aims to ensure that the flow remains stationary and to capture wind turbulence exclusively. In line with these practices, and following (Stickland, 2012; for Standardization, 2004) recommendations the data recorded by the sonic anemometer were organized into a 10-minute mean time series.

To ensure high data quality the wind data obtained by all instruments were carefully cleaned to eliminate any missing values, errors, or outliers. The data associated with less than 5%, not a number (NaN) values were interpolated using a spring metaphor method (D'Errico, 2017). Additionally, any records that exhibited a mean wind speed bias exceeding 10 $m{\cdot}\mathrm{s}^{-1}$ between the lidar instruments were excluded from the analysis. This step ensures that only data points with a reasonable level of agreement between the lidar instruments are considered.

To guarantee the accuracy of the analysis and account for the influence of turbulence intensity and atmospheric stability, an additional step was taken in data selection. The turbulence intensity, being inversely proportional to the mean wind speed, can lead to overestimated values at low wind speeds. Therefore, samples with mean wind speed values below 6 $m{\cdot}\mathrm{s}^{-1}$ were removed to mitigate this issue. Moreover, identification of atmospheric stability was not possible due to a lack of direct access to eddy covariance measurements, the exclusion of low wind speeds further ensures the removal of both strongly stable and unstable stratification patterns.

Furthermore, to directly compare data obtained by two individual scanning lidars and two 3D sonic anemometers time series between the two sets of data were synchronized in frequency and time. It is important to note that only the along-beam velocity component v_r is considered for this comparison. The lidar instruments directly measure the along-beam radial velocity, whereas, for the sonic anemometers data, v_r is reconstructed using equation 2.5. Lastly, the data was divided into five different wind sectors 3.1.

During the analysis of the data collected by the sonic anemometers, a horizontal positioning misalignment was identified. This misalignment may have been caused by various factors such as installation error or mast deformation. The double rotation technique was applied to compensate for the tilt in both masts for sonic anemometer sensors. This technique involves rotating the coordinate system twice to align the measurement axes with the vertical (w) and horizontal (v) directions. The first rotation aligns the mean flow direction

with the x-axis, while the second rotation forces the v and w components to be zero, resulting in a new coordinate system where the y-axis points in the cross-wind direction and the z-axis points upwards (Wilczak et al., 2001).

By applying the double rotation technique, the tilt angle of the sensors is adjusted in a way that horizontal and vertical wind components become aligned with the actual directions of the wind flow. The use of this technique is common practice in wind engineering and atmospheric sciences and is effective in compensating for misalignment in the sensors (Wilczak et al., 2001).

3.4.1 Power Spectra Density and Coherence analysis

To study turbulent wind fluctuations, the selected data from sonic anemometers and wind lidars are detrended by removing any linear trend present in the data. The PSD of the wind velocity fluctuations analysis is based on 10-minute wind data records obtained from the sonic anemometer. The PSD is calculated using Welch's algorithm method (Welch, 1967) with 3 segments of 200 s length and 50% overlapping as suggested by (Carter et al., 1973). Resulting in the frequency band ranging from 5 mHz to 10 Hz. The use of multiple segments is required to reduce the large measurement noise and bias associated with the use of the modified periodogram estimate (Kristensen & Kirkegaard, 1986; Saranyasoontorn et al., 2004).

However, it is important to note that for finite-duration signals increasing the number of overlapping segments comes at the cost of reduced frequency resolution and increased the lowest frequency recorded. In the present study, the use of 3 overlapping segments for a single time series is considered appropriate (Midjiyawa et al., 2021b). In addition, to smooth out the PSD in the high-frequency range, a non-overlapping block average is applied, using 60 equally spaced blocks on a log scale. Lastly, the single velocity spectra were ensemble averaged using the arithmetic mean.

In this study, the computation of co-coherence is performed in two parts. The first part involves the use of 10-minute time series obtained from sonic anemometers. This analysis focuses on examining the co-coherence of turbulence based on the measurements from sonic anemometers alone. The second part aims to validate the capability of pulsed Doppler wind lidar instruments in capturing the lateral co-coherence of turbulence. To achieve this, the time series data from two wind-pulsed lidars and two sonic anemometers are synchronized in time. The co-coherence analysis in this part utilizes time series data with a duration ranging from 30 to 50 minutes.

In the first part of the co-coherence analysis, to optimize the computation process, the sampling frequency of the data is decimated by a factor of 5,

resulting in a sampling frequency of 4 Hz. The co-coherence is then calculated using Welch's algorithm method with 15 overlapping segments, each with a 50% overlap. The computation of two-point cross-spectra requires a larger number of segments compared to one-point spectra. This is necessary due to the increased bias and random error associated with the estimation of the cross-spectrum. To further refine co-coherence estimates, a smoothing technique was applied in the high-frequency range with 60 non-overlapping blocks on a log scale. Lastly, the co-coherence estimates were ensemble averaged using the arithmetic median.

In the second part, the co-coherence is established following the same Welch method approach as in the first part. The key difference is that the sampling frequency of the sonic anemometer is decimated by a factor of 20, resulting in the same frequency of 1Hz for both instruments and with 6 overlapping segments. Additionally, 6 overlapping segments are used to achieve a trade-off between minimizing random measurement errors and maximizing frequency resolution.

Chapter 4

Results and Discussions

4.1 Integral Turbulence Characteristics

The parameters presented in table 4.1 are commonly used in atmospheric boundary research and wind energy applications to characterize the turbulence of the wind field. The normalized standard deviation of turbulent velocity fluctuations can provide valuable statistical insights, particularly when analyzed by sector. By splitting the data into chosen sectors, we can better understand the distribution of these fluctuations and their behavior across different regions.

The analysis exclusively considers samples with a mean wind speed exceeding 6 $m{\cdot}\mathrm{s}^{-1}$ in order to align the obtained results with non-neutral atmospheric conditions. The turbulence statistics for a single point averaged across a sector, and their corresponding standard deviations are provided for analysis. The standard deviations are denoted by the $+/-$ symbol. The values of σ_u/u_*, σ_v/u_*, and σ_w/u_* are a measure of the variability of the wind speed in the streamwise, lateral, and vertical directions, respectively, normalized by the friction velocity u_*.

In neutral atmospheric conditions, the σ_w/u_* ratio value varies depending on the terrain. For flat and uniform terrain typical values for the σ_w/u_* ratio range from 1.10 to 1.40, as noted by Panofsky & Dutton (1984). In rolling terrain, this ratio ranges from 1.20 to 1.24 Meanwhile, Kaimal & Finnigan (1994) observed that the σ_w/u_* ratio remains largely unchanged from upwind to hilltop. Based on this, they suggested a ratio σ_w/u_* value of 1.25. This study found that the σ_w/u_* ratio values range from 1.21 to 1.50, with some values slightly higher than those reported in the literature. This higher spread may be attributed to the presence of turbulence sources such as buildings and a lighthouse situated to the east of the LidarW, as well as the proximity of the seashore and escarpment.

The interpretation of σ_u/u_* and σ_v/u_* values is challenging due to the observed scatter. Topographical features have a greater impact on the horizontal turbulence components compared to the vertical component (Midjiyawa et al., 2021a). The horizontal velocity spectrum, under neutral conditions, contains low-frequency eddies with higher energy than the vertical velocity spectrum, as noted by Panofsky et al. (1982). This low-frequency range is more sensitive to hills and roughness changes than the high-frequency range, as explained by Frank (1996). As a result, rough terrain is expected to have a wider range of values for σ_u/u_* and σ_v/u_* than the flat terrain.

In flat and uniform terrain under neutral atmospheric conditions, Kaimal & Finnigan (1994) suggest ratios of σ_u/u_* as 2.4 and σ_v/u_* as 1.9. While Panofsky & Dutton (1984) suggest values of 2.39 and 1.92 and in rolling terrain 2.65 and 2.00, respectively. Therefore, it is expected that in certain sectors, these ratio values may be higher than the literature values due to the presence of the escarpment and the lighthouse. In the present study, the σ_u/u_* ratios are in the range from 1.96 to 2.57 while the σ_v/u_* ratios range from 1.46 to 2.13. However, results presented in the table 4.1 indicates lower than expected values in wind sectors 120°-180° and 300°-330°. Lower values may be attributed to the presence of non-neutral atmospheric conditions during the measurement process. In a similar study conducted by Midjiyawa et al. (2021a) lower than expected values for σ_u/u_* ratio were linked to flow along mountain slope. Considering these findings, it might be assumed that the wind sector ranging from 300° to 330°, which is associated with an escarpment, exhibits wind flow characteristics similar to those observed in flow along mountain slopes. This similarity in flow behavior could account for the lower values observed in this sector.

The previously discussed mean values of the ratios σ_w/u_* = 1.25 and σ_u/u_* = 2.4 can be used to derive the ratio of σ_w/σ_u by dividing the two values. This results in

$$\frac{\sigma_w}{\sigma_u} = 0.52 \tag{4.1}$$

According to Solari & Piccardo (2001) in flat and homogeneous terrain, a ratio $\sigma_w/\sigma_u \approx 0.5$ is expected. On the other hand, the turbulence model proposed by Kaimal et al. (1972), with correction in the inertial sub-range, leads to a ratio σ_w/σ_u = 0.57 (Kaimal & Finnigan, 1994).

In the present study, the ratio of σ_w/σ_u has been observed to vary from 0.59 to 0.63 for the west mast and 0.53 and 0.61 for the east mast. The variation is more pronounced in different angular sectors around the mast compared to the spatial distribution between the two masts. The variation in different sectors refers to the difference in the values of σ_w/σ_u in different angular

sectors around the mast, while the spatial distribution refers to the distribution of these values between two masts. The variation in different sectors is larger than in spatial distribution because the terrain and topography around the mast may be more complex and heterogeneous in certain angular sectors compared to others. Different sectors are affected by different roughness scales such as the ocean, lighthouse, and escarpment, leading to more variability in the turbulence intensity. Conversely, the effects of these obstacles over two spatial positions tend to average out, resulting in less turbulence intensity variability.

Results of the analysis of the σ_w/σ_u also reveal that several values exceeded the theoretical values of σ_w/σ_u. However, these values are consistent with previous measurements conducted in complex topography (Midjiyawa et al., 2021a) and on the shores of Bjørnafjorden site (Cheynet et al., 2018a).

Additionally, an interesting finding is observed in the wind sector 210°-300° reflecting wind flow from the ocean side. In this sector a value of σ_w/σ_u = 0.53 was obtained measured by the east mast. This value aligns with the ratio of σ_w/σ_u = 0.53 observed in offshore wind measurements conducted at a height of 80 m above the surface under neutral conditions(Cheynet et al., 2017a).

As previously mentioned, in flat and homogeneous terrain, Kaimal & Finnigan (1994) suggested values of the ratio σ_v/u_* = 1.9 and σ_u/u_* = 2.4, they can be used to calculate the ratio of σ_v/σ_u by dividing the two values. Consequently, the resulting

$$\frac{\sigma_v}{\sigma_u} = 0.79 \tag{4.2}$$

According to the findings of Solari & Piccardo (2001), the expected range for the ratio of σ_v/σ_u in flat terrain is between 0.67 and 0.88. In the present study, the measured values for the ratio of σ_v/σ_u range from 0.75 to 0.91. Most of the values are in agreement with the range reported by Solari & Piccardo (2001), except for one value measured by the west mast in the 300°-330° sector, which exceeds the expected range with a value of 0.91. This might be due to an escarpment in the west area which modified the wind flow.

The findings presented in table 4.1 suggest that the terrain in the study area is not as flat as expected. The presence of diverse structures, including buildings, a lighthouse, and an escarpment, contributes to local flow separation. Additionally, the data collection process across different sectors introduces further variability. It is important to note that the requirement for a mean wind speed above 6 $m{\cdot}\mathrm{s}^{-1}$ implies that data might have been collected at different times, potentially leading to variations in atmospheric conditions. Another significant factor contributing to the observed variability is the variation in

surface roughness among sectors. Specifically, the wind direction in the 220°-330° reflects offshore wind, while the other sectors encompass land with distinct characteristics such as grass, rocks, and buildings. These differences between ocean and land features cause significant variations in the roughness length as a function of the wind direction.

Table 4.1: Statistical properties of turbulent velocity fluctuations expressed as the normalized standard deviation for different wind sectors. Derived from data collected by West and East sonic anemometers from 16.03.2020 to 30.03.2020. Only samples associated with $\bar{u} > 6\ m{\cdot}\mathrm{s}^{-1}$ are considered. (For the number of samples for sectors refer to table 4.2).

Mast	Sector (°)	σ_u/u_*	σ_v/u_*	σ_w/u_*	σ_v/σ_u	σ_w/σ_u
West	120-180	1.96±0.17	1.46±0.15	1.23±0.09	0.75±0.07	0.63±0.06
East	120-180	1.99±0.15	1.49±0.14	1.21±0.08	0.75±0.07	0.61±0.05
West	180-210	2.39±0.28	1.85±0.33	1.41±0.17	0.77±0.09	0.60±0.06
East	180-210	2.41±0.42	1.89±0.36	1.44±0.16	0.78±0.07	0.61±0.08
West	210-300	2.45±0.59	1.97±0.41	1.34±0.22	0.81±0.14	0.56±0.08
East	210-300	2.38±0.59	1.82±0.32	1.23±0.18	0.82±0.59	0.53±0.08
West	300-330	2.28±0.37	2.08±0.52	1.34±0.22	0.91±0.16	0.60±0.10
East	300-330	2.30±0.59	1.91±0.49	1.23±0.30	0.88±0.34	0.56±0.15
West	330-20	2.57±0.45	2.13±0.44	1.50±0.21	0.83±0.13	0.59±0.08
East	330-20	2.52±0.40	2.04±0.42	1.47±0.19	0.82±0.13	0.60±0.13

The wind rose in figure 4.1 provides information on the distribution of turbulence intensity across different wind speeds at each mast location. The wind rose allows the determination of the prevailing wind direction and speed, along with the frequency of occurrence for different wind directions and speeds. Additionally, comparing the two wind roses any spatial differences in wind speed and turbulence intensity can be identified between the two locations.

Figure 4.1 illustrates the presence of three distinct sectors for both the west and east masts, characterized by varying levels of turbulence intensity. The resulting turbulence intensity in figure 4.1 can be classified into two groups for the west and east mast. In two cases, the west and east sonic anemometers display similar and consistent values of turbulence intensity. This suggests that the observations are more likely influenced by flow disturbances rather than measurement errors or the mast structure itself.

The first group which contains the highest turbulence intensity values is observed in the wind sector ranging from 130° to 195° and 345°-15°. In this case, turbulence intensity values (I_u) are observed approximately between

13%-27%. The second group observed in the wind sector ranging from 200° to 340° with approximately turbulence intensity values I_u = 4%-13%.

The highest turbulence intensity values in the first group are observed for the south wind, specifically within the wind direction range of 160° to 185°, as indicated by both sonic anemometer measurements. This finding suggests that the increased turbulence intensity might be attributed to the presence of flow separation downstream and the wake generated by the surrounding buildings and a tall lighthouse. According to the research conducted on the wake characteristics of tall buildings (Hertwig et al., 2019), it is highly probable that the high turbulence intensity measurements are influenced by the wake phenomenon.

When considering the first group as a whole, it is observed that the wind direction originates from the land. In the case of wind coming from the land, the diurnal cycle may be stronger. This is because the land heats up and cools down more rapidly compared to the sea. The temperature differences between land and sea can lead to varying atmospheric stability, which in turn affects turbulence intensity. Therefore, wind from the land may have higher values of turbulence intensity.

Considering the second group when the wind originates from the sea, this group experiences less influence from the diurnal cycles. The absence of a diurnal cycle in wind from the sea indicates that there is relatively less change in atmospheric stability within a span of 1-2 weeks. As a result, the turbulence intensity for wind from the sea tends to be more consistent over time compared to wind from the land.

Additionally, the first and second groups have different roughness lengths which is an important factor that affects turbulence intensity. For instance, the smaller roughness scale of the seawater compared to land masses leads to less turbulence in wind from the sea. It is worth noting that the wind sector spanning from 345° to 15°, characterized by turbulence intensity values of 13%-18%, and wind originating from the north, cannot be categorized as offshore wind due to the higher turbulence intensity observed compared to offshore environments.

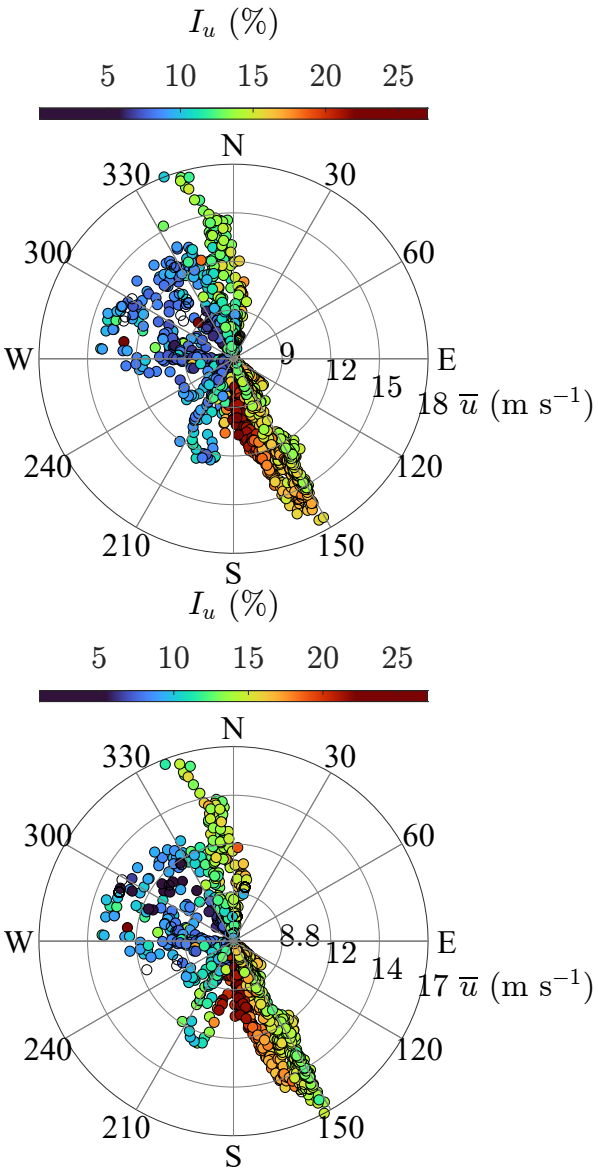

Figure 4.1: Wind rose for the turbulence intensity for the along wind component as a function of mean wind speed and direction. Recorded by sonic anemometers for the mast west (upper panel)(Total samples 1467) and mast east (lower panel) (Total 1478 samples). Data was collected from 16.03.2020 to 30.03.2020. Only samples associated with $\bar{u} > 6\ m{\cdot}\mathrm{s}^{-1}$ are considered. (For the number of samples for sectors refer to table 4.2).

Figure 4.2 documents the distribution of the mean angle of attack (AoA) with respect to mean wind speed. By comparing measurements for the west and east sonic anemometers, it is possible to identify any spatial differences in along-wind direction flow between the two locations. Observations from

the west sonic anemometer indicate the presence of two distinct sectors in the southeast and northwest directions. Within these sectors, the mean AoA ranges from -5.15° to 19.87° for different wind directions. These significant differences in mean AoA values within the southeast and northwest sectors strongly suggest the presence of a tilt angle error for the west sonic anemometer.

This error is likely due to horizontal misalignment of the sonic anemometer or tilt in the mast structure, which introduces a bias in the measured wind direction. As a result, it becomes necessary to apply a double rotation correction to compensate for this misalignment or tilt in the horizontal positioning of the anemometer. It is worth noting that although the differences in mean AoA for the east sonic anemometer are smaller, the double rotation correction is applied to both sonic anemometers to ensure consistent measurements.

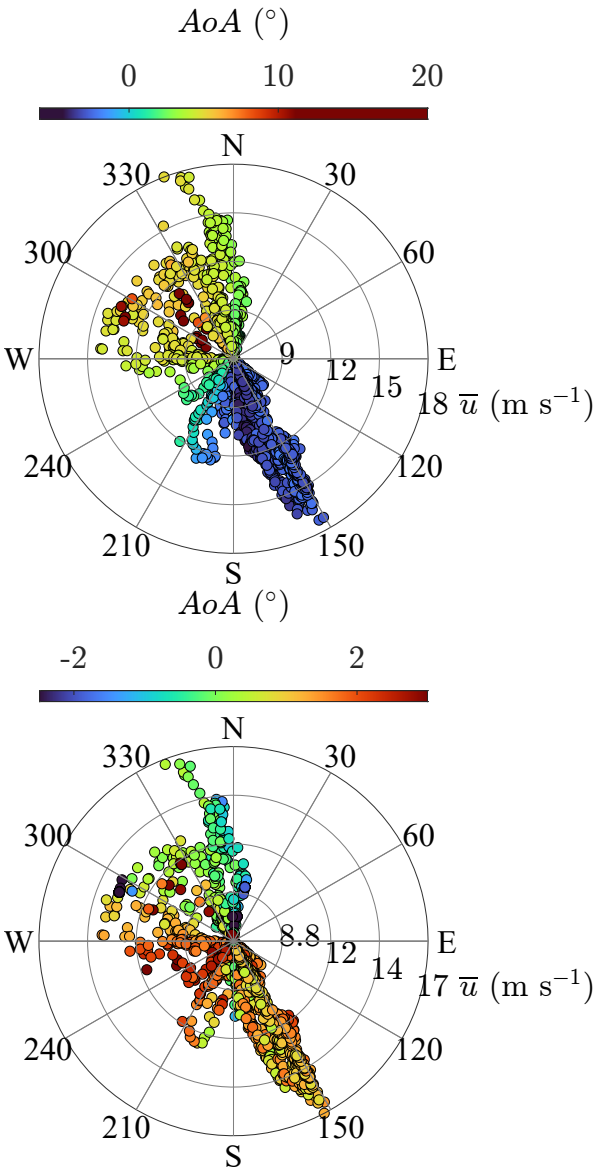

Figure 4.2: Wind rose for the mean angle of attack (AoA) as a function of mean wind speed and direction. Recorded by sonic anemometers for the mast west (upper panel)(Total samples 1467) and mast east (lower panel) (Total 1478 samples). Data was collected from 16.03.2020 to 30.03.2020. Only samples associated with $\bar{u} > 6\ m{\cdot}s^{-1}$ are considered.(For the number of samples for sectors refer to table 4.2).

Figure 4.3 documents the relationship between the standard deviation of vertical velocity fluctuations σ_w and the standard deviation of along-wind velocity fluctuations σ_u. The ratio values of σ_w/σ_u are discussed in Table 4.1

for various wind directions.

The figure for both sonic anemometer measurements shows two distinct groupings, namely 180°-340°, and 340°-180°. It can be observed that σ_w/σ_u values are lower for wind directions from 180°-340° (from the sea) compared to wind directions from 340°-180° (from the land).

Furthermore, the highest σ_w/σ_u values are observed for wind directions ranging from 140°-180°. This suggests that the downstream effect of the lighthouse may significantly influence these values, particularly at lower mean wind speeds from 9 $m{\cdot}\mathrm{s}^{-1}$ to 12$m{\cdot}\mathrm{s}^{-1}$. The turbulence and variations in roughness are likely contributing factors to the observed impact on the σ_w/σ_u values.

Notably, for wind directions ranging from 340°-180° and mean wind speeds between 12 $m{\cdot}\mathrm{s}^{-1}$ and 15 $m{\cdot}\mathrm{s}^{-1}$, the σ_w/σ_u values exhibit less variation and demonstrate greater consistency compared to wind directions from 180°-340° within the same mean wind speed range. This trend is particularly evident in the measurements obtained by the west sonic anemometer, which is located closer to the hill. The lower consistency observed with wind directions from 180°-340° may be attributed to the presence of the hill.

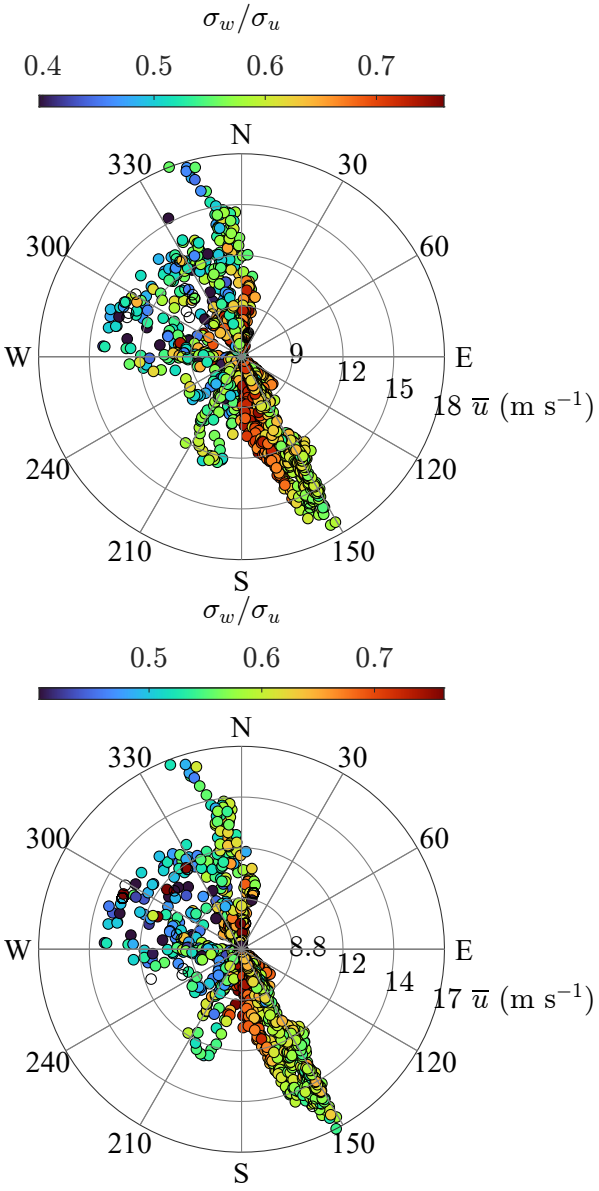

Figure 4.3: Wind rose for the ratio σ_w/σ_u of the standard deviation of the vertical velocity fluctuations and along-wind velocity fluctuations as a function of mean wind speed and direction. Recorded by sonic anemometers for the mast west (upper panel)(Total samples 1467) and mast east (lower panel) (Total 1478 samples). Data was collected from 16.03.2020 to 30.03.2020. Only samples associated with $\bar{u} > 6\ m{\cdot}\mathrm{s}^{-1}$ are considered. (For the number of samples for different sectors refer to table 4.2).

Table 4.2: Number of samples for different sectors obtained by the West and East sonic anemometer from 16.03.2020 to 30.03.2020 at 11 meters above the ground ($\sim$ 28 m asl.). Only samples associated with $\bar{u} > 6\ m{\cdot}\mathrm{s}^{-1}$ are considered.

	120°-180°	180°-210°	210°-300°	300°-330°	330°-20°
West	750	92	207	87	383
East	746	82	283	67	363

4.2 One-point Velocity Spectra of Turbulent Wind Fluctuations

Figure 4.4 shows the ratios of S_w/S_u for five different wind sectors for the West (upper panel) and East (lower panel) masts. In neutral atmospheric conditions, the theory of local isotropy (Kolmogorov, 1941) predicts that the ratio of S_w/S_u reach a value of 1.33 within the inertial-subrange. However, when the flow is distorted by buildings, lighthouses, or/and other obstacles, a lower value of the ratio S_w/S_u is expected.

In figure 4.4 it is observed that for two specially separated places only one wind sector ranging from 180° to 210° reached the theoretical value of 4/3. For the west mast, this wind sector is the only which reached the theoretical value. However, the ratio value surpasses the value of 4/3 as the frequency increases. Similarly, for the east mast wind sector, 180°-210° is the sector to attain and surpass the value of 4/3. However, the increase above the value of 4/3 at higher frequencies for the east mast is relatively slight compared to the west mast. This suggests that it is less likely that observation for the west mast is related to an instrumental error. This might be linked to the presence of an escarpment in close proximity to the west mast. Where the west mast could be influenced more by the wind conditions upstream of the escarpment. A similar issue is observed in the study conducted by Midjiyawa et al. (2021b) where the ratio values of S_w/S_u were significantly higher compared to the theoretical value of 4/3 due to the presence of the hill.

In the wind sector ranging from 120° to 180°, for the west mast, the ratio value of 1.32 is observed at $f_r \geq 5.5$. In contrast, for the east mast, the maximum value of ratio S_w/S_u is 1.28 which is reached at frequency $f_r \geq 6$. Several factors may contribute to the discrepancy observed in the ratio S_w/S_u, resulting in smaller values compared to the theoretical expectation, particularly in the case of measurements from the east mast. One possible reason is the influence of the wake created by the lighthouse on the downwind flow in the

wind sector of 120°-180°, particularly affecting the east mast measurements. The presence of the lighthouse generates turbulence and disturbances in the wake, potentially altering the wind flow patterns and influencing the observed ratio. Additionally, it is worth considering that the wind flow records may also be affected by the structure of the mast itself.

The wind sector ranging from 300° to 330° is the second wind sector where the theoretical value of 4/3 is attained, but solely for the east mast. Specifically, the value of 4/3 is achieved at $f_r > 7$. In contrast, the west mast exhibits a maximum ratio value of S_w/S_u of 1.28 at frequencies exceeding $f_r > 3$. The lower ratio value observed for the west mast could be attributed to the interaction between the sea and land, where the sudden presence of higher friction velocity leads to a deceleration of the wind.

The wind sector ranging from 210° to 300° for both the west and east masts does not reach the theoretical values of the ratio S_w/S_u. However, it is observed that the east mast is more affected, exhibiting lower values of the ratio S_w/S_u compared to the west mast. This discrepancy could be attributed to the presence of the ocean or an escarpment in the vicinity of the east mast. This could influence the wind flow patterns and contribute to the observed differences. It is worth noting that the number of samples 4.2 available for the east mast in this sector is higher, indicating potentially decreased statistical variability. Despite the slightly lower values of ratio S_w/S_u observed for both masts, the east mast exhibits an increasing pattern toward the theoretical value at $f_r > 3$. In contrast, the west mast demonstrates a decreasing pattern deviating from the theoretical value.

The wind sector ranging from 330° to 20° for both west and east masts values of the ratio S_w/S_u remains below 4/3. The observations for the east mast display slightly higher values of the ratio S_w/S_u, indicating the flow distortion for the west mast measurements. In the present case, it is observed that the ratio values of S_w/S_u for the west mast in this particular sector are the smallest compared to all other sectors. This suggests that the flow distortion in the west mast measurements could be attributed to a combination of factors, including the presence of an escarpment and a sudden change in roughness scale from a smooth ocean surface to a rough terrain of the rocks and grass.

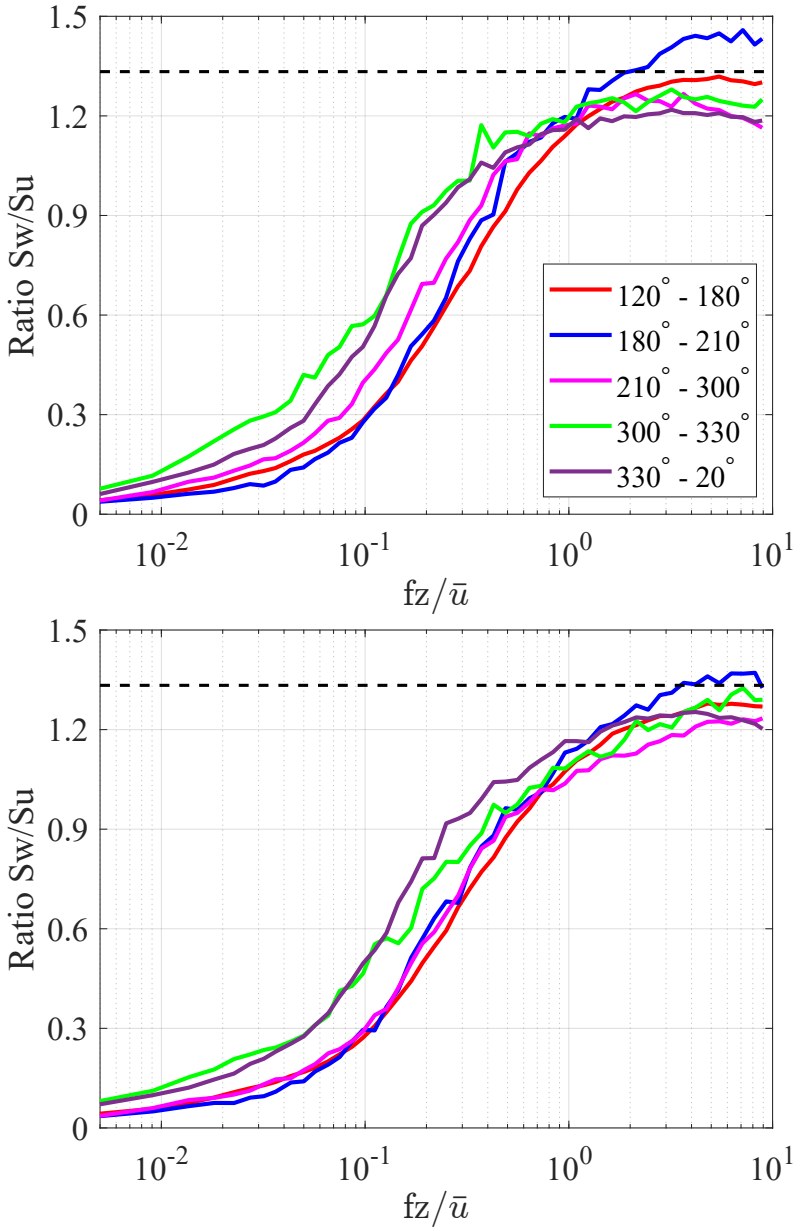

Figure 4.4: Power spectra density ratio of S_w/S_u vertical and along wind velocity components. Recorded by sonic anemometers for the mast west (upper panel) and mast east (lower panel). Data was collected from 16.03.2020 to 30.03.2020. Only samples associated with $\bar{u} > 6\ m{\cdot}\mathrm{s}^{-1}$ are considered. The dashed line shows the theoretical ratio value of 1.33. (For information on the number of samples for sectors, refer to Table 4.2).

The power spectra densities of the along-wind velocity 4.5, across-wind velocity 4.6, and vertical-wind velocity 4.7 are analyzed using data from two sonic anemometers spaced 20 meters apart and located at 28 meters asl. The data was divided into five sectors across different regions to better understand the distribution of turbulent wind fluctuations associated with different wind directions.

Figure 4.5 shows the results of the analysis of different along-wind PSD estimates for two masts. The sector from 330° to 20° exhibits the highest normalized S_u value of 1.33 at a normalized frequency of 0.02 ($fz/\bar{u}$) among the west sonic anemometer measurements. Meanwhile, for the east sonic anemometer measurements, the sector ranging from 180° to 210° shows the highest normalized S_u value of 1.43 at the normalized frequency 0.05 ($fz/\bar{u}$).

The power spectral density estimates for both the west and east sonic anemometers showed the lowest normalized S_u values in the sector ranging from 120° to 180°, with normalized S_u values of 0.83 and 0.84 at the normalized frequency of 0.09 ($fz/\bar{u}$) and 0.06 ($fz/\bar{u}$), respectively. The lower normalized S_u values observed in the power spectral density (PSD) estimates could be attributed to the presence of six residential buildings, including a 16.5-meter-tall lighthouse, in the southeast area from the sonic anemometers. These obstacles are likely causing turbulence in the flow, resulting in reduced wind speeds and higher turbulence in the downwind direction. The consistent observation of this pattern across both mast locations suggests that this effect is not limited to a particular measurement site.

In sector 300°-330° for the west and east sonic anemometers measurements, the low-frequency range of the PSD is much larger than predicted by the Kaimal model. In sector 300°-330° for both the west and east sonic anemometer measurements, it is observed that the low-frequency range of the power spectral density (PSD) is larger than what is predicted by the Kaimal model. This discrepancy may be attributed to several factors. Firstly, since this study did not eliminate non-neutral conditions it might be showing a predominance of unstable stratification. Secondly, the presence of an escarpment can induce flow separation, resulting in higher normalized S_u values in the sector. Additionally, the wind direction in this sector has a narrow range of 30° and is less frequently observed 4.2, resulting in more variable energy levels compared to other directions.

The sector from 210°-300° exhibit a similar pattern to that of the sector from 300°-330°. One noteworthy difference is that the measurements from east and west sonic anemometers in the sector from 210°-300° follow the Kaimal spectra at normalized frequency $fz/\bar{u} > 0.04$. This may be attributed to the wind flow, which follows the coastline and resembles the reference Kaimal

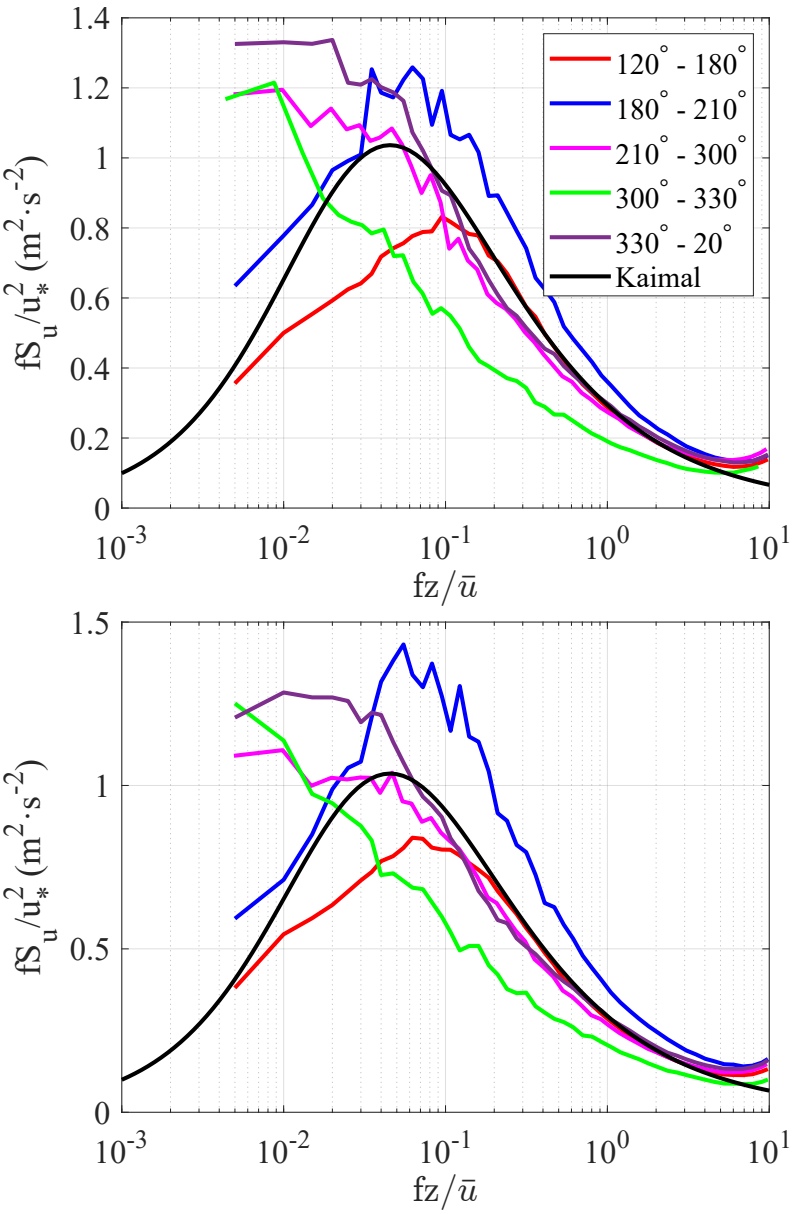

Figure 4.5: Power spectra density estimate of along-wind component recorded by sonic anemometers for the mast west (upper panel) and mast east (lower panel). Data was collected from 16.03.2020 to 30.03.2020. Only samples associated with $\bar{u} > 6\ m{\cdot}\mathrm{s}^{-1}$ are considered. (For information on the number of samples for different sectors, refer to Table 4.2).

spectra. Additionally, this sector has a larger number of samples, which may contribute to the overall robustness of the observed pattern.

Figure 4.6 documents the power spectra density of the across-wind velocity. The findings can be grouped into two groups based on the west and east sonic anemometers. The first group exhibits higher normalized S_v values at normalized frequencies $fz/\bar{u} < 10^{-1}$ compared to the fitted Kaimal spectrum. Observation shows that wind directions ranging from 180° to 210° have exceeded the Kaimal model. The highest normalized S_v value of 0.95 in this group is found in the wind sector ranging from 300° to 330° at frequency $fz/\bar{u} < 10^{-2}$. This significant value might be attributed to wind affected by the coastline. Additionally, this sector may indicate a predominance of unstable stratification, where the buoyancy force induces convection near the sea, leading to increased turbulence intensity.

The second group exhibits lower normalized S_v values at normalized frequencies $fz/\bar{u} < 10^{-1}$ compared to the fitted Kaimal spectrum. This group is characterized by a single wind direction ranging from 120° to 180°. The wind flow in this direction is likely influenced by the wake generated from the nearby building and lighthouse.

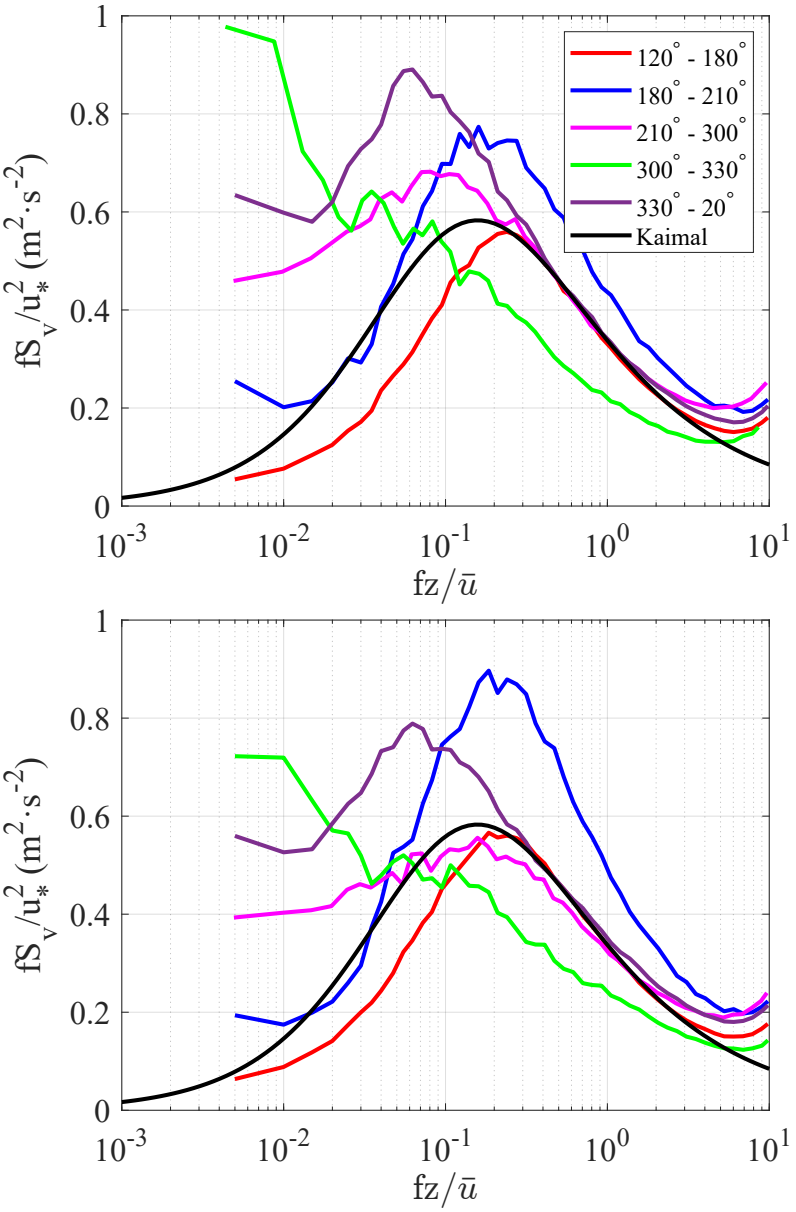

Figure 4.6: Power spectra density estimate of across-wind component recorded by sonic anemometers for the mast west (upper panel) and mast east (lower panel). Data was collected from 16.03.2020 to 30.03.2020. Only samples associated with $\bar{u} > 6\ m{\cdot}\mathrm{s}^{-1}$ are considered. (For information on the number of samples for different sectors, refer to Table 4.2).

Figure 4.7 documents the power spectra density of the vertical-wind velocity. In comparison with 4.5 and 4.6, the vertical wind velocity for both sonic anemometer measurements demonstrate a closer agreement with the empiri-

cal Kaimal model for normalized S_w, particularly at normalized frequencies $fz/\bar{u} < 10^{-1}$. However, two wind sectors 180°-210° and 330°-20° exhibit significantly higher normalized S_w values compared to the predicted Kaimal spectrum. It is worth noting that this finding is consistent with the observations found for 4.5 and 4.6 in the same sectors. The significantly higher values observed in the wind sectors ranging from 180° to 210° and from 330° to 20° align across all three power spectra densities S_u, S_v, and S_w.

The power spectral density for the vertical-wind velocity in wind sectors 120°-210° and 210°-300° for both sonic anemometer measurements have good agreement with the Kaimal model across all frequency ranges. However, the wind sector ranging from 300° to 330° exhibits lower normalized S_w values at frequencies $fz/\bar{u} > 10^{-1}$ compared to the Kaimal model.

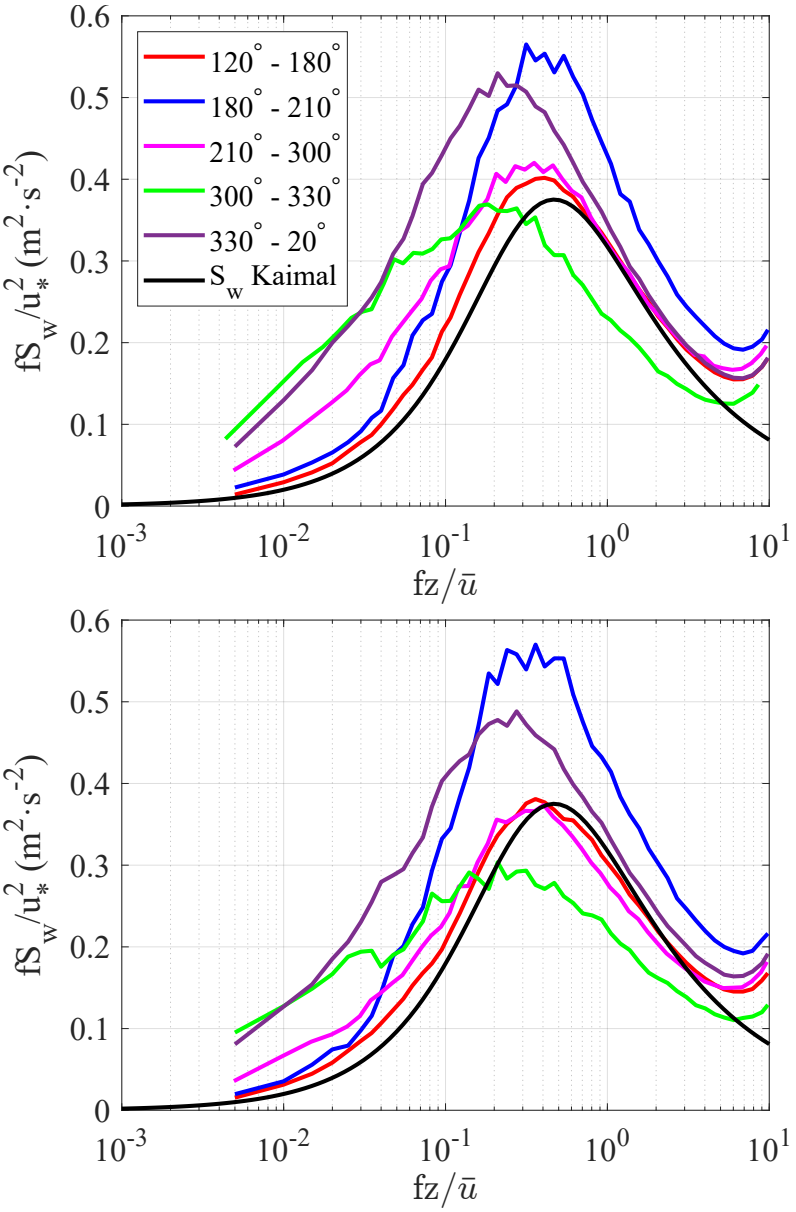

Figure 4.7: Power spectra density estimate of vertical wind component recorded by sonic anemometers for the mast west (upper panel) and mast east (lower panel). Data was collected from 16.03.2020 to 30.03.2020. Only samples associated with $\bar{u} > 6\ m{\cdot}\mathrm{s}^{-1}$ are considered. (For information on the number of samples for different sectors, refer to Table 4.2).

4.3 Coherence of Turbulence Analysis using Sonic Anemometers

As mentioned earlier, the co-coherence analysis provides more insights into wind loading, while quad-coherence is often neglected in the field of wind engineering due to its limited relevance. This chapter analyzes co-coherence observation obtain from two sonic anemometers with a separation distance of 20 meters. The figure, 4.8 documents lateral co-coherence estimates of along wind component. The co-coherence estimates are divided into different sectors to determine which wind direction is associated with the highest co-coherence values.

In the wind sectors, ranging from 180° to 210° and from 210° to 300° the smallest co-coherence values observed are $\gamma_u = 0.35$ and $\gamma_u = 0.5$ respectively, at frequencies $k < 10^{-2}\ m^{-1}$. These co-coherence values at a low-frequency range are considered to be small for a separation distance of 20 meters.

In a similar study conducted by Cheynet et al. (2016), which analyzed laeral co-coherence using sonic anemometer data, it was observed that the co-coherence value for the along-wind component reached $\gamma_u = 1$ at low frequencies with a separation distance of 24 meters. Additionally, for separation distances of 72 and 96 meters, the co-coherence values were close to $\gamma_u < 1$.

Remarkably, a notable co-coherence agreement is observed among the sectors 120°- 180°, 300°-330°, and 330°-20° where the co-coherence value reaches $\gamma_u = 0.5$ at frequencies $k < 10^{-2}\ m^{-1}$. However, it is important to note that despite this agreement, the co-coherence values in these sectors still remain relatively small.

The small co-coherence values observed in figure 4.8 may be influenced by various factors. The co-coherence estimate in the sector 180°-210° might be attributed to the turbulent flow induced by the presence of the lighthouse. Figure 4.1 indicates that turbulence values in this sector can reach up to 25% for a mean wind speed of 9 $m{\cdot}\mathrm{s}^{-1}$. The magnitude of co-coherence tends to decrease with increasing turbulence intensity. This is because higher turbulence intensity leads to increased spatial and temporal variability in the flow, making it more challenging to maintain co-coherence between two points. The increased variability can result in non-homogeneous turbulence, further impacting the ability to maintain co-coherence between points in the flow.

The study by (Midjiyawa et al., 2021b) observed that the fitted decay coefficient of the Davenport model did not demonstrate a clear sensitivity to the roughness length and fetch, specifically for lateral separation. This finding suggests that these factors may have a limited influence on the co-coherence

estimates. These findings support the observations in figure 4.8 as the co-coherence estimates in different sectors show a similar pattern, except for the sector 180°-210° affected by the presence of buildings and lighthouse.

Where the slightly lower co-coherence value in the sector 210°-300° compared to the sectors 120°- 180°, 300°-330°, and 330°-20° could be explained by the choice of the averaging interval for data analysis. This choice may have resulted in the smoothing out of low-frequency fluctuations. Additionally, it is important to take into account that the atmospheric conditions during the measurements may not have been stable. This can lead to non-homogeneous turbulence characteristics, despite the relatively short distance between the anemometers.

The negative co-coherence values were found to be small indicating slight anti-correlation between the turbulent along-wind velocity components at two spatially separated points. The strongest negative co-coherence is observed in sectors 180°-210°, 210°-300°, and 30°0-330° with values of $\gamma_u =$ -0.176, $\gamma_u =$ -0.184, and $\gamma_u =$ -0.126, respectively, at frequencies k = 0.045 (m^{-1}), k = 0.06 m^{-1}, and k = 0.075 m^{-1}. This can be explained by the fact that the line formed by the two masts is not perpendicular to the west wind. Therefore, the negative co-coherence in these sectors can be associated with a time lag introduced by the opposite phase of the turbulent velocity components measured at two different spatial points.

The transition zone where co-coherence values begin approaching zero has been observed at k = 0.2 m^{-1}. The co-coherence estimates of the along the wind velocity component approach zero at high frequencies because the turbulent structures at high frequencies are much smaller in size than the separation distance between the two sensors. As a result, the sensors do not measure the same structures at the same time. The correlation between the measurements decreases, resulting in co-coherence values converging to zero.

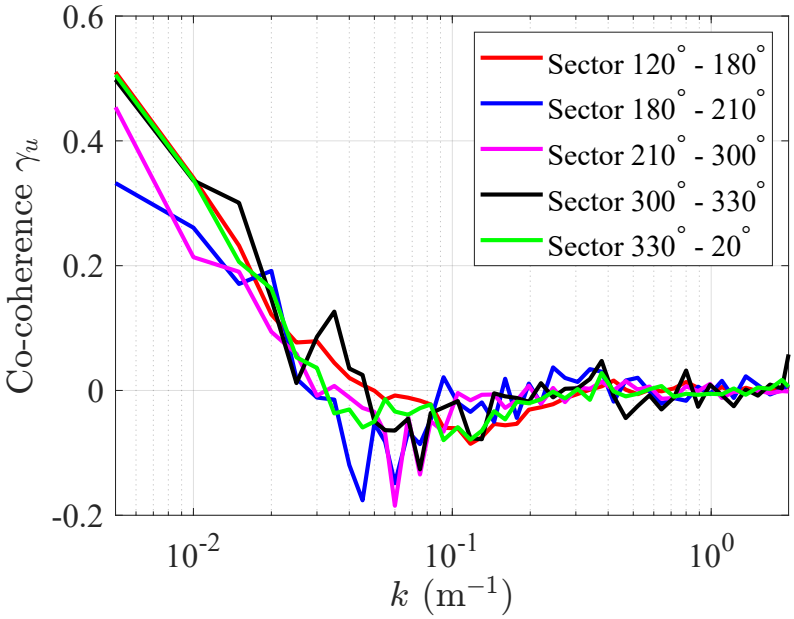

Figure 4.8: Lateral co-coherence of turbulence for along-wind velocity $\gamma_u =$ as a function of frequency between sonic anemometer west and east with a separation distance of 20 m in different sectors. Data was collected from 16.03.2020 to 30.03.2020. Only samples associated with $\bar{u} > 6\ m{\cdot}\mathrm{s}^{-1}$ are considered. (For information on the number of samples for different sectors, refer to table 4.3).

Table 4.3: The number of samples obtained between the sonic anemometers west and east in different wind sectors for lateral along wind velocity component co-coherence $\gamma_u =$ analysis. Data was collected from 16.03.2020 to 30.03.2020. Only samples associated with $\bar{u} > 6\ m{\cdot}\mathrm{s}^{-1}$ are considered.

Sector	120°-180°	180°-210°	210°-300°	300°-330°	330°-20°
West & East	740	77	193	61	336

4.4 Synchronized Data Analysis for Coherence of Turbulence Validation

To ensure a reliable and consistent comparison between the data captured by the sonic anemometers and the lidar instruments, only the along-beam velocity component v_r is considered in this chapter.

Figure 4.9 compares the mean value and standard deviation of the along-beam component v_r obtained from sonic anemometers and lidars where all wind directions are considered. In figure 4.9, the x-axis and y-axis represent different combinations of measurements obtained from lidar and sonic anemometer instruments.

A high degree of correlation between the mean values of $\overline{v_r}$ is observed from two lidars and two sonic anemometers in the top left panel of figure 4.9. The coefficient of determination $R^2 > 0.99$ indicates that along-beam mean velocity $\overline{v_r}$ is almost identical for two different instruments, at least at the location of the masts. However, the measurements between LidarW-MastW have a higher degree of correlation compared to LidarN-MastW.

The top right panel of figure 4.9 compares the standard deviations of along-beams values recorded by two lidars and two sonic anemometers. Data measurements noise associated with σ_{v_r} is observed to be higher for LidarN when compared to the data obtained from the sonic anemometers. Measurements between LidarN and MastE have a broader spread and several outliers resulting in a lower degree of correlation and in coefficient of determination value $R^2 = 0.902$.

A possible reason for the incompatibility observed in both top panels of figure 4.9 might be the slightly inhomogeneous flow within the 25-meter-long probe volume used for the lidar's wind measurements. The lidars measure the wind flow perpendicular to the line crossing the two mast positions within a thin cylinder of 25 m in length. Compared to sonic anemometers, the along-beam wind velocity fluctuations and variability are larger measured with the lidar instruments.

In the two middle and bottom panels of figure 4.9, only sonic anemometers and lidars data are compared highlighting a comparison of measurements within the same instrument type. The lidar measurements show a lower degree of correlation in $\overline{v_r}$ measurements with a value of R^2 = 0.991 and also a lower degree of correlation σ_{v_r} with a value of R^2 = 0.916, compared to the sonic anemometers which have values of R^2 = 0.996 and R^2 = 0.976, respectively.

According to Cheynet et al. (2021) findings for the COTUR campaign the lidar data exhibit more noise for the southern flow than the northern flow, potentially because of the flow separation present downstream of the hill.

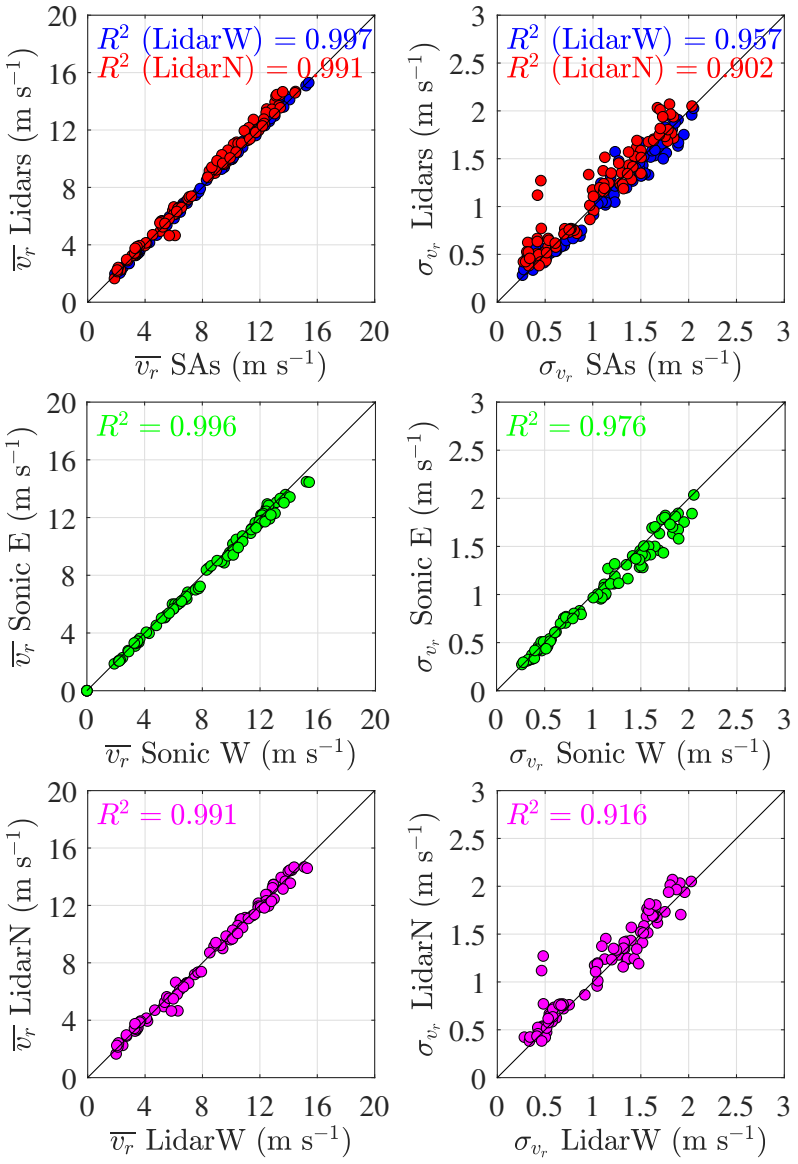

Figure 4.9: The coefficient of determination R^2 comparison of along-beam mean velocity component values $\overline{v_r}$ (left panels) and standard deviations σ_{v_r} of along-beam velocity component values (right panels) obtained from two sonic anemometer sensors and two scanning lidars. Synchronized data is based on a lidar duration of 30-50 min between 17.03.2020 and 30.03.2020.Only samples associated with $\bar{u} > 6\ m{\cdot}s^{-1}$ are considered

A comparable pattern is found by observations in figure 4.1 where higher turbulence intensity I_u values are observed in south-southeast directions and lower I_u values are observed in the northwest directions for both masts.

Therefore, to ensure a more accurate measurement comparison and categorization of turbulent wind structure, it is essential to separately compare the co-coherence estimates obtained from lidars and sonic anemometers for the different wind sectors. The sectors were selected with the objective of gathering as many high-quality samples as achievable while also maintaining a narrow wind sector range. To be able to compare co-coherence measurements from two different instruments directly.

For direct high-quality data comparison of co-coherence estimates data, v_r values associated with not realistic data are eliminated and only data containing less than 5%, (NaN) are used. Following data synchronization and quality testing, only three sectors remained.

These sectors are 180°-210°, 300°-330°, and 330°-20°. Despite the fact that three of five sectors passed the quality check sector 300°-330° has only three co-coherence samples. Therefore, only two main sectors are used to validate the ability of pulsed Doppler wind lidar instruments to capture the lateral co-coherence of turbulence.

It is important to note that the purpose of the comparison is to evaluate the applicability of a pulsed lidar system to capture the co-coherence of turbulence exclusively. Thus, co-coherence is estimated without attempting to describe it in terms of a function as atmospheric stability, mean wind speed, crosswind distance, or upstream roughness length. Consequently, this study does not attempt to fit an empirical coherence model to ensemble-average co-coherence estimates.

Wind sectors that remained are 180°-210° and 330°-20°. Figure 4.10 presents two-time series of 50 minutes where measurements of 2 spacial points are recorded for wind directions between 330° and 20°. The time series obtained from LidarW exhibit excellent agreement with the records from MastW. However, LidarN demonstrates higher measurement noise compared to MastE, and the reason for this discrepancy is unknown.

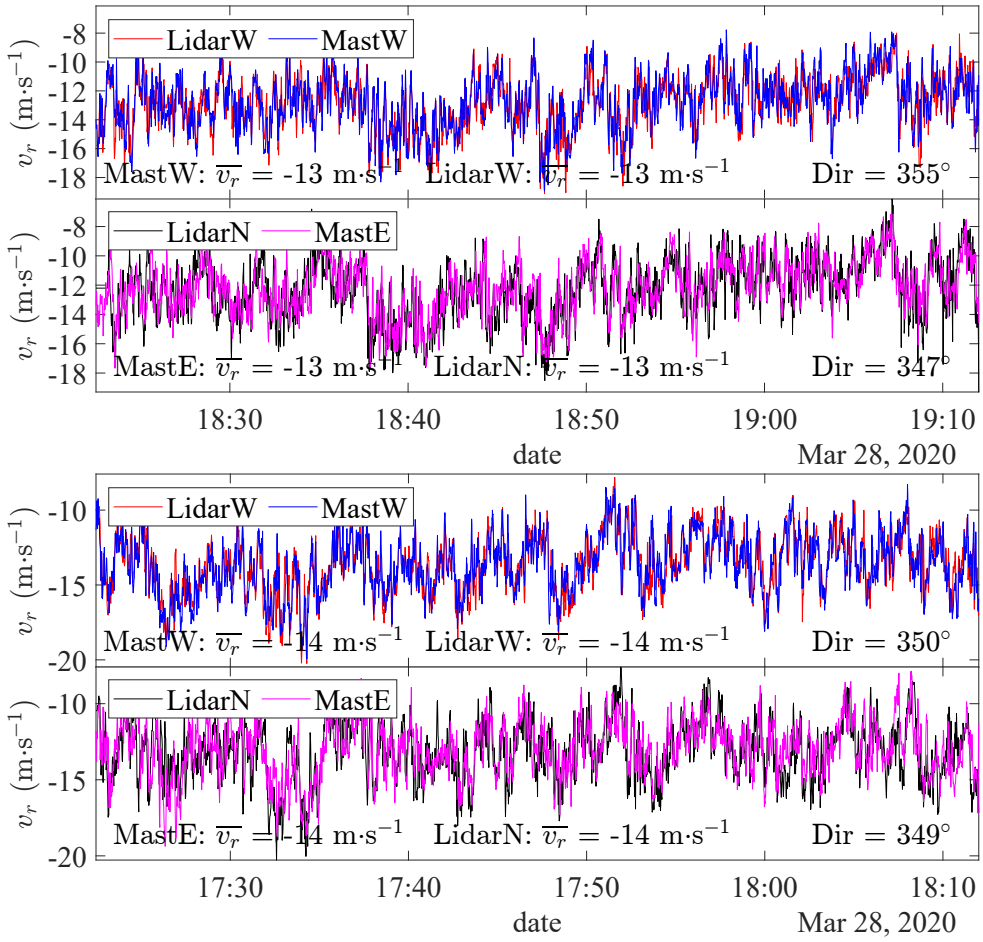

Figure 4.10: Synchronized time-series of along-beam radial velocity v_r component obtained by synchronized two pulsed lidars and two sonic anemometers for wind sector 330°-20°. Date: 28.03.2020.Only samples associated with $\bar{u} > 6\ m{\cdot}s^{-1}$ are considered

Twelve-time series of high-quality data, leading to 10 hours of wind velocity records with mean wind direction between 330° and 20° is utilized to determine co-coherence for this sector. An ensemble-averaged co-coherence estimate based on 10 hours of selected data is presented in figure 4.11. Where the measurements from the sonic anemometer and Lidar data are presented in four different groupings providing measurements at two spatial positions with a 20-meter separation distance.

Observations in figure 4.11 exhibit an excellent agreement of co-coherence of along-beam velocity γ_{v_r} estimated using LidarW and sonic anemometer on MastE, as well as between the two sonic anemometers. There is an excellent agreement across the entire frequency range, with only minor inconsistencies

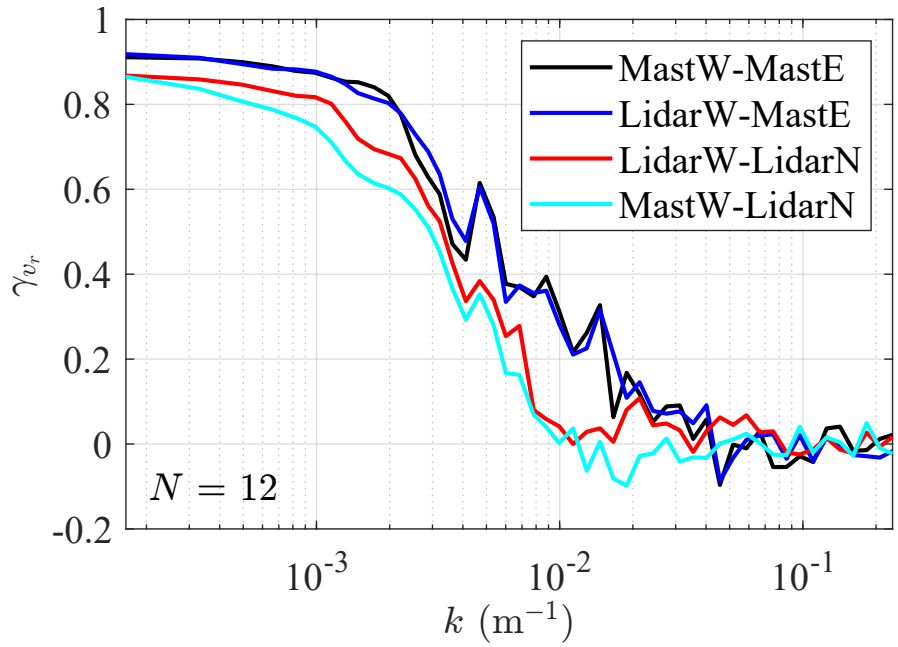

Figure 4.11: Later co-coherence γ_{v_r} for along beam velocity component measured $\overline{v_r}$ averaged over 12 synchronized time-series of duration 30-50 min. Measured by dual pulsed lidar system and two sonic anemometers with a separation distance of 20 m for wind sector 330°-20° 330-20.Only samples associated with $\bar{u} > 6\ m{\cdot}\mathrm{s}^{-1}$ are considered.

observed at higher frequencies $k \geq 0.066\ m^{-1}$

However, these inconsistencies are negligible and do not significantly affect the overall results. It could be claimed that a direct spatial averaging effect on the probe length of 25 meters is not observed for LidarW in this sector. This implies that the size of the volume being measured is proportional to the scale of the turbulence being studied at the MastE.

Lower than expected co-coherence γ_{v_r} values with measurements associated with LidarN are observed in figure 4.11. Low co-coherence γ_{v_r} values at the low-frequency range may be affected by noisy records from LidarN. On the contrary, despite the noisy records from LidarN, consistent patterns, and similar behavior are observed in the measurements between LidarW and LidarN, as well as MastW and LidarN.

When considering south-southeast wind directions, which are associated with noisy Lidars data the co-coherence estimates are lower due to the influence of the turbulent wind field. Figure 4.12 compares turbulence intensity for the v_r component between sonic anemometers and lidars for all wind directions.

The individual comparison of instruments is shown in the middle and

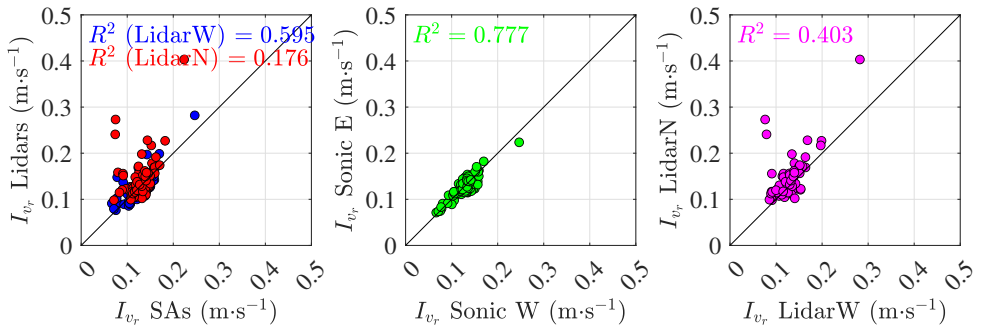

Figure 4.12: The coefficient of determination R^2 comparison of turbulnce intensity measurements for along-beam component I_{v_r} obtained by two lidars and two sonic anemometers. The left panel indicates obtained measurements for LidarW-MastW and LidarN-MastE combinations. The middle and right panels indicate obtained measurements for the same instrument type. Synchronized data is based on a lidar duration of 30-50 min between 17.03.2020 and 30.03.2020.Only samples associated with $\bar{u} > 6\ m{\cdot}s^{-1}$ are considered

right panels of the figure 4.12. It is observed that the turbulence intensity data obtained from the sonic anemometers exhibit a higher degree of correlation, with an R^2 value of 0.777, compared to the lidars, which show a lower degree of correlation with an R^2 value of 0.403. This may be attributed to the higher temporal resolution of the sonic anemometer, which captures small-scale structures better than Lidar. Additionally, lidar systems may have a different spatial resolution and may not be sampling the same volume of air as the sonic anemometers, as seen in the case of LidarN.

The right panel of figure 4.12 compares the turbulence intensity data of two lidars and two sonic anemometers. LidarW shows better agreement with MastW with a degree of correlation of R^2 = 0.595 compared to LidarN and MastE where a degree of correlation is R^2 = 0.176 observed. This is as expected due to the noisy measurements identified earlier for LidarN.

Figure 4.13 presents two-time series of 50 minutes records of two sonic anemometers and two lidars for wind directions between 120° and 180°. For these wind directions, the lidars data were observed to be noisier compared to northern flows 4.10. As previously discussed this might be due to high induced turbulence intensity by the lighthouse or the hill. Therefore, the mean wind flow might not always be homogeneous and can adversely affect co-coherence measurements for this wind direction.

However, it is worth noting that long-term records at the site indicate that the most frequent winds blow parallel to the coast, thereby providing numerous opportunities to collect high-quality data (Cheynet et al., 2021). Fifty-six-

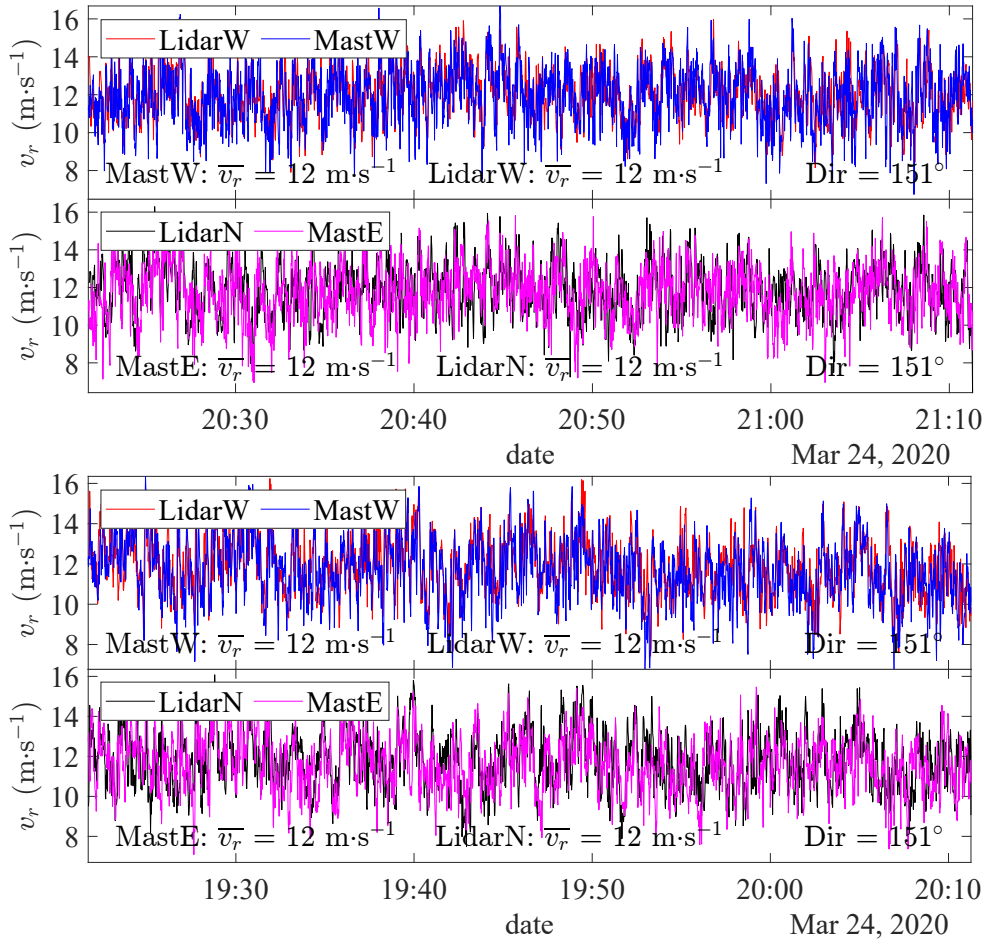

Figure 4.13: Synchronize time-series of along-beam radial velocity v_r component obtained by two lidars and two sonic anemometers instruments for wind sector 120°-180°. Date: 28.03.2020.Only samples associated with $\bar{u} > 6$ $m{\cdot}\mathrm{s}^{-1}$ are considered

time series of high-quality data, leading to 30 hours of wind velocity records with mean wind direction between 120° and 180° is utilized to determine co-coherence for this sector.

An ensemble-averaged co-coherence estimate based on 30 hours of selected data is presented in figure 4.14. As expected, the observed co-coherence values (γ_{v_r}) are smaller than for the northerly wind direction. Indicating a weaker correlation between two spatial points being measured in wind sector 120°-180°.

However, measurements between LidarW and MastE show lower agreement with measurements obtained between MastW and MastE. Where the co-coherence γ_{v_r} estimates between MastW and MastE are slightly higher compared to LidarW and MastE.

This could be attributed to the more heterogenous wind flow in this wind direction due to the presence of various obstacles associated with different roughness lengths. Additionally, measurements obtained from wind sector 120°-180° most likely are affected by the downstream and the wake due to the presence of the tall lighthouse. Respectively, resulting in less good quality data obtained by the instruments in this southerly wind direction. This could be also due to factors such as the presence of noise in the LidarW records and spatial averaging effects where values associated with low frequency may have been filtered out. At low frequencies, where wind fluctuations occur over a longer spatial scale the spatial averaging process can result in a blurring or dampening effect. This blurring effect tends to reduce the amplitude of low-frequency variations and can lead to the filtering out of certain values associated with those frequencies. Nevertheless, a consistent pattern is observed across all frequencies between these measurements. Both measurement combinations capture the negative part of co-coherence at the same frequency as well as approach unity at a higher frequency.

The co-coherence measurements between the two lidars exhibited a small value $\gamma_{v_r} \neq 0.49$ for low frequencies. This could be attributed to the influence of the spatial averaging effect, which might have been affected by high wind turbulence induced by the presence of the escarpment and lighthouse. The turbulent flow patterns created by these features can lead to increased spatial variability and inconsistency in the measured data, contributing to the reduced co-coherence values observed at low frequencies.

The lowest co-coherence value $\gamma_{v_r} \neq 0.41$ is observed in the measurement combination between MastW and LidarN at low frequencies, and the reasons behind this significantly low co-coherence remain an open question. It is also plausible to assume potential spatial inhomogeneity between the two measured locations. Yet, the measurement combination obtained between the two lidars shows good agreement with measurements recorded between MastW and LidarN in middle and high frequencies.

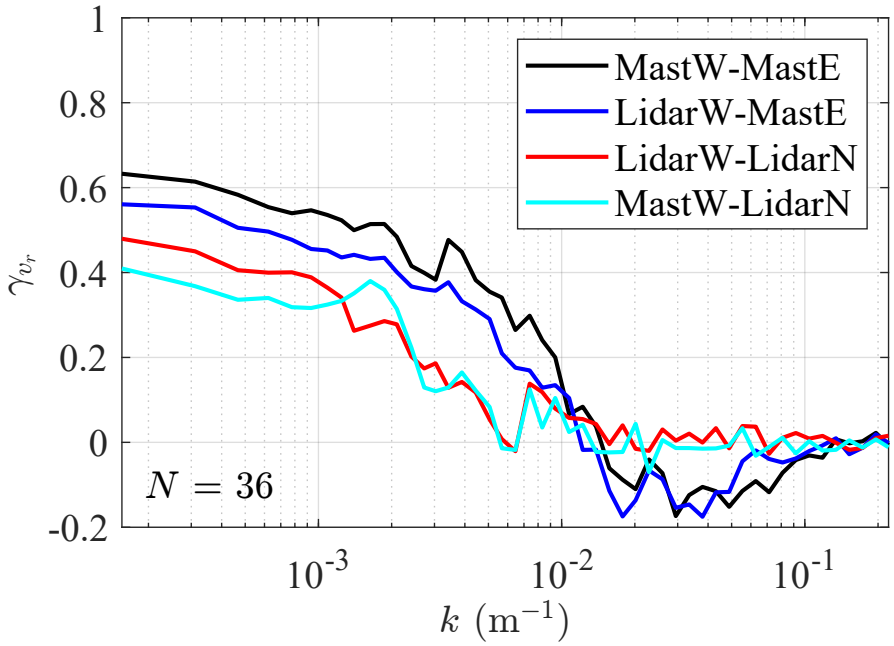

Figure 4.14: Later co-coherence γ_{v_r} for along beam velocity component $\overline{v_r}$ averaged over 36 synchronized time-series of duration 30-50 min. Measured by dual pulsed lidar system and two sonic anemometers with a separation distance of 20 m for wind sector 120°-180°.Only samples associated with $\bar{u} > 6\ m{\cdot}\mathrm{s}^{-1}$ are considered.

Chapter 5

Conclusions and Future Works

This study compared wind measurements obtained from two Scanning Doppler wind lidars and two 3D sonic anemometers deployed near Obrestad lighthouse. The main focus was on evaluating the capability of pulsed Doppler wind lidar instruments to capture the lateral coherence of turbulence. The validation of the lidar against the sonic anemometer instrument, particularly in terms of coherence, was effectively demonstrated by analyzing the real part of coherence.

This thesis also examined the impact of various terrains on the statistics of wind measurements, specifically focusing on single and 2-point statistics. The investigation provided insights into the variability and characteristics of wind flow patterns across different roughness scales. Additionally, a brief discussion of the performance of pulsed wind lidar in measuring turbulence intensity was conducted, comparing the data collected from the two different instruments across all wind sectors associated with different terrain categories.

The results revealed that only wind sectors aligned with northerly or southerly wind directions passed the data quality test and had appropriate sample numbers with the flow being approximately parallel to the lidar beams.

Therefore two wind sectors were considered, specifically the wind sector ranging from 330° to 20° and from 120° to 180°. The potential effect of the terrain on the local flow conditions was more limited for the northerly wind sector and it was identified as the most suitable for validating the dual pulsed lidar system's ability to capture lateral coherence of turbulence.

In the northerly wind direction, both LidarN and LidarW data exhibited less measurement noise and demonstrated better agreement with the two sonic anemometer data compared to the southerly wind direction. The potential source of measurement noise for the southerly wind direction was discussed and linked to the downstream effects of the hill and to the wake generated by the presence of the lighthouse and several buildings. The measurement noise was also observed in turbulence intensity measurements using lidars. The brief

analysis of the turbulence intensity measurements was discussed in terms of the amount of variation in the data. The results revealed a higher degree of correlation in measuring turbulence intensity between LidarW-MastE compared to LidarN-MastW. Emphasizing the presence of measurement noise in data collected by LidarN. The comparison between the individual instruments highlights that the sonic anemometer is more reliable for turbulence intensity measurements.

The determined co-coherence values obtained by the lidar and sonic anemometer data with a separation distance of 20 meters for both wind sectors were found to be lower than expected. The co-coherence values did not reach a value of 1 at low-frequencies as suggested by theory. Particularly low co-coherence values were found for southerly wind direction between MastW-LidarN and LidarW-LidarN. The actual reason for the low co-coherence value is unknown, but it may be related to spatial inhomogeneity. The least affected co-coherence measurements were found between LidarW-MastE and MastW-MastE for the northerly wind directions. Comparing the two co-coherence estimates showed negligible differences, indicating that spatial averaging did not significantly affect the estimation of co-coherence, at least during the encountered weather conditions.

This thesis aimed to validate lidar measurements against the sonic anemometer measurements, and the focus was on how well measurements do overlap. The turbulence intensity comparison between the individual instruments highlights that the sonic anemometer is more reliable for turbulence intensity measurements. However, despite the limited length of data used and low co-coherence values, a significant performance of LidarW was identified in capturing the co-coherence over all frequency ranges for the measurements in the wind sector ranging from 330° to 20°. The solid agreement between the LidarW and the anemometers suggests that the pulsed wind lidar using the probe volume of 25m demonstrates the ability to capture the lateral co-coherence of turbulence for the along-wind component. However, the findings also indicated that if one of the two lidars contains some measurement noise, the co-coherence could be significantly underestimated.

This validation can be considered the first step in estimating co-coherence using pulsed Doppler wind lidar. Contributing to alternative and accessible methods for measuring the coherence of turbulence and assessing its ability to provide measurements at altitudes relevant to offshore wind turbines.

To the best of the author's knowledge, the field of WindScanners and their capability to measure coherence requires further exploration, making this thesis a starting point for future research. In future studies, analyzing a larger dataset to minimize data deviation and maximize data variability is advisable.

Moreover, considering atmospheric stability as a significant factor that impacts coherence would be a necessary next step in validating the capture coherence of turbulence using WindScanners. Therefore, for a more comprehensive future investigation into the scanning wind lidar's potential in capturing turbulence coherence, it is highly recommended to accurately estimate atmospheric stability by using a 3D sonic anemometer and storing the sonic temperature data.

Furthermore, to explore additional possibilities for estimating coherence using pulsed lidar, it is suggested to expand the measurement setup. This can be achieved by using more than two masts equipped with sonic anemometers and pointing scanning lidars toward them. For example, within the context of this study, adding an extra mast with a sonic anemometer and a separation distance of 20 meters from one of the existing masts would be beneficial. Additionally, incorporating an additional scanning lidar pointing toward the extra mast would enable the investigation of three separation distances. This setup would allow for the comparison of coherence between two separation distances of 20 meters, as well as the investigation of an additional larger separation distance of 40 meters. By implementing this extended configuration, the research can be conducted in a more detailed and reliable manner, providing valuable insights into the relationship between different separation distances and coherence.

Chapter 6

Appendix

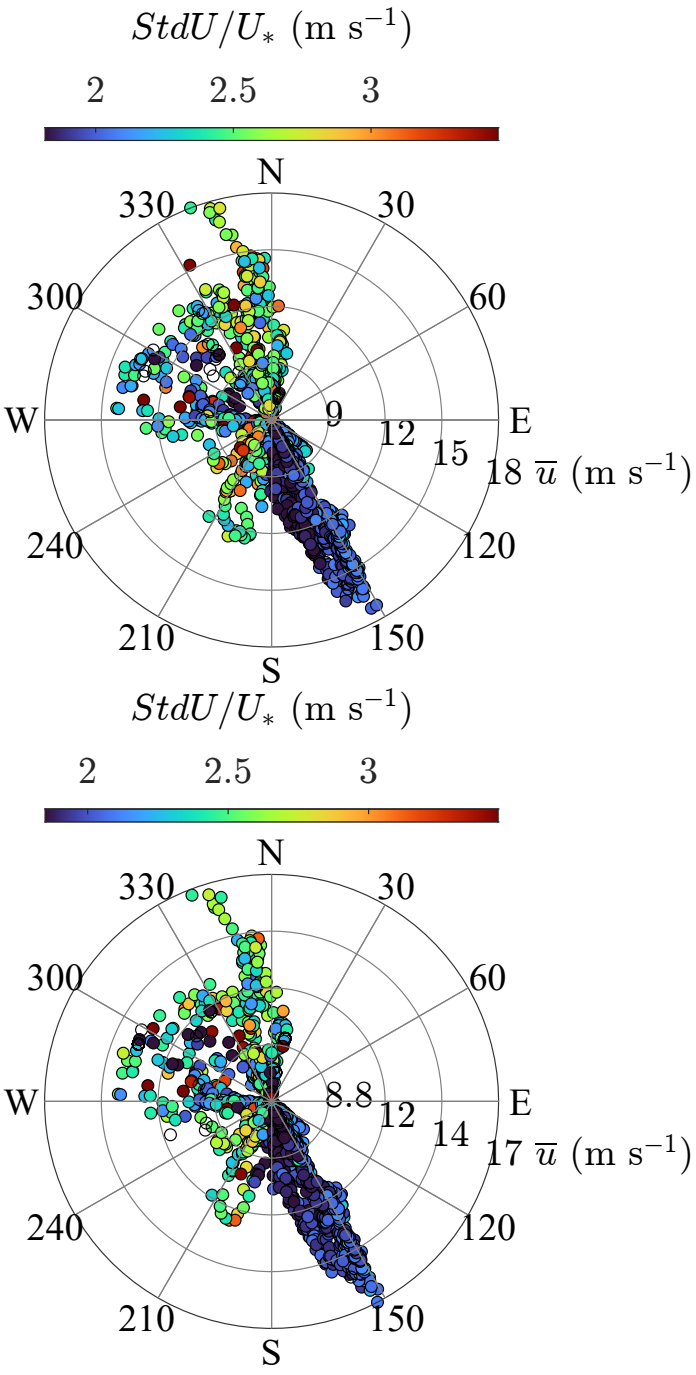

Figure 6.1: Wind rose for the ratio σ_w/u_* data was collected from 16.03.2020 to 30.03.2020. Sonic anemometer west (top panel) and sonic anemometer (bottom panel). Only samples associated with $\bar{u} > 6\ m{\cdot}s^{-1}$ are considered.(For the number of samples for different sectors refer to table 4.2).

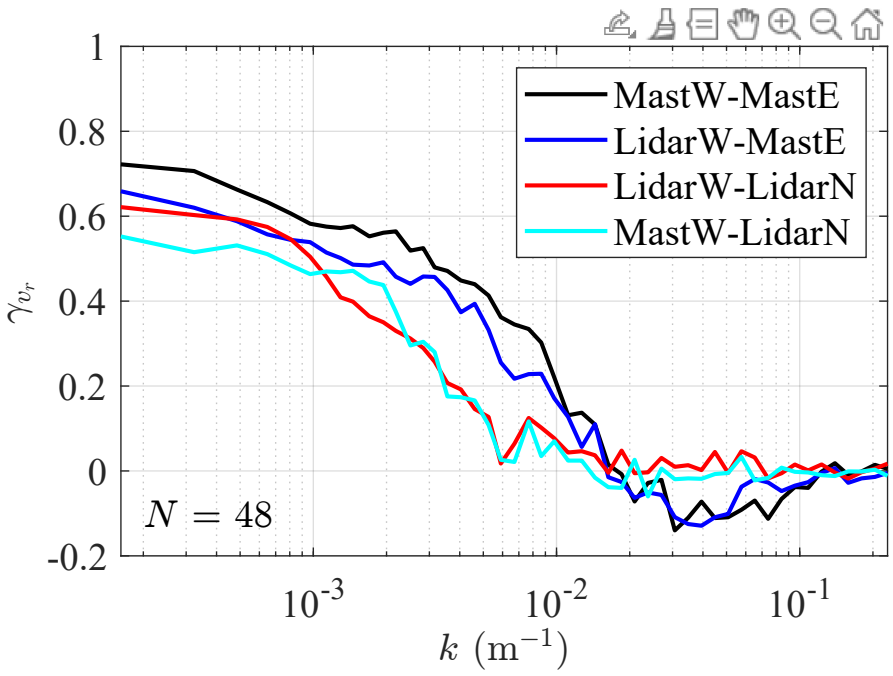

Figure 6.2: Later co-coherence γ_{v_r} for along beam velocity component $\overline{v_r}$ measured for all wind directions (0° to 360°).

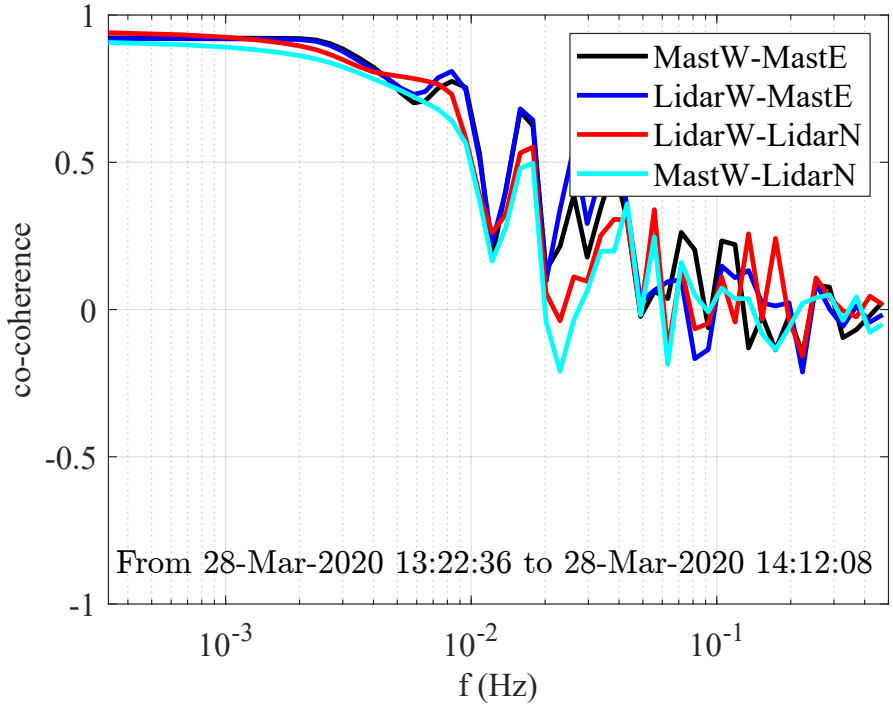

Figure 6.3: Later co-coherence γ_{v_r} for along beam velocity component $\overline{v_r}$ for single 50min time-series.

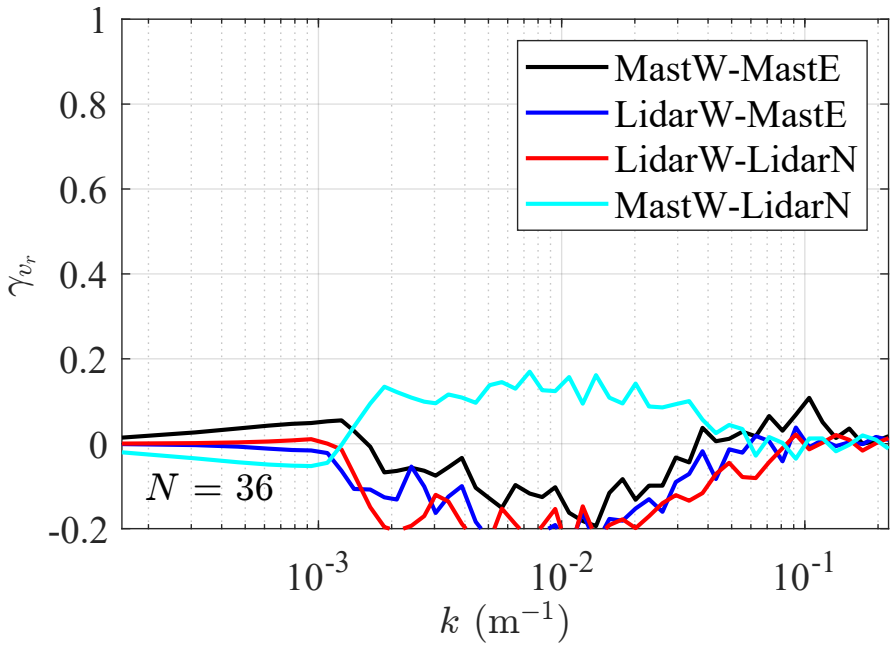

Figure 6.4: Later quad-coherence γ_{v_r} for along beam velocity component $\overline{v_r}$ measured for wind directions (120° to 180°).

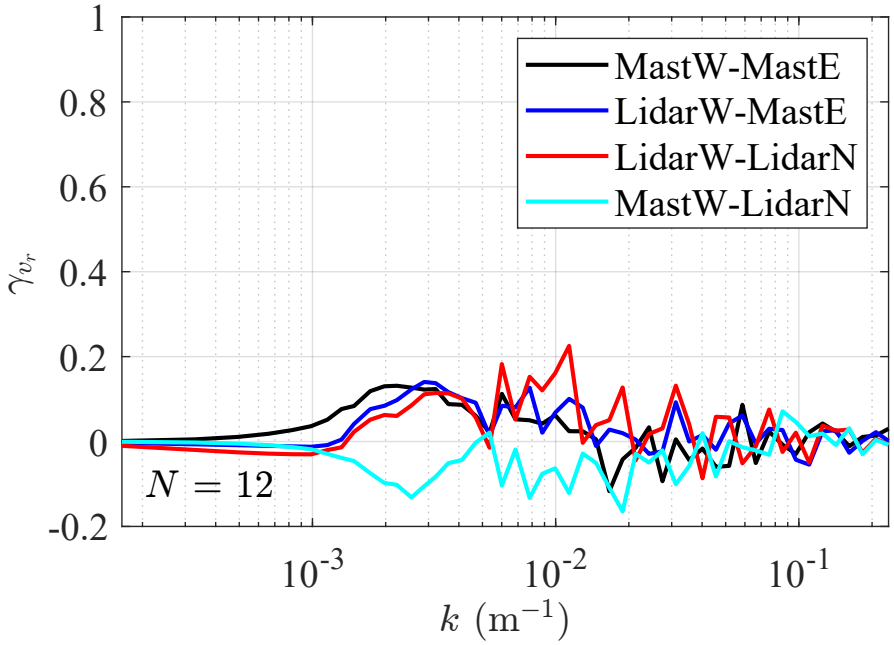

Figure 6.5: Later quad-coherence γ_{v_r} for along beam velocity component $\overline{v_r}$ measured for wind directions (320° to 20°).

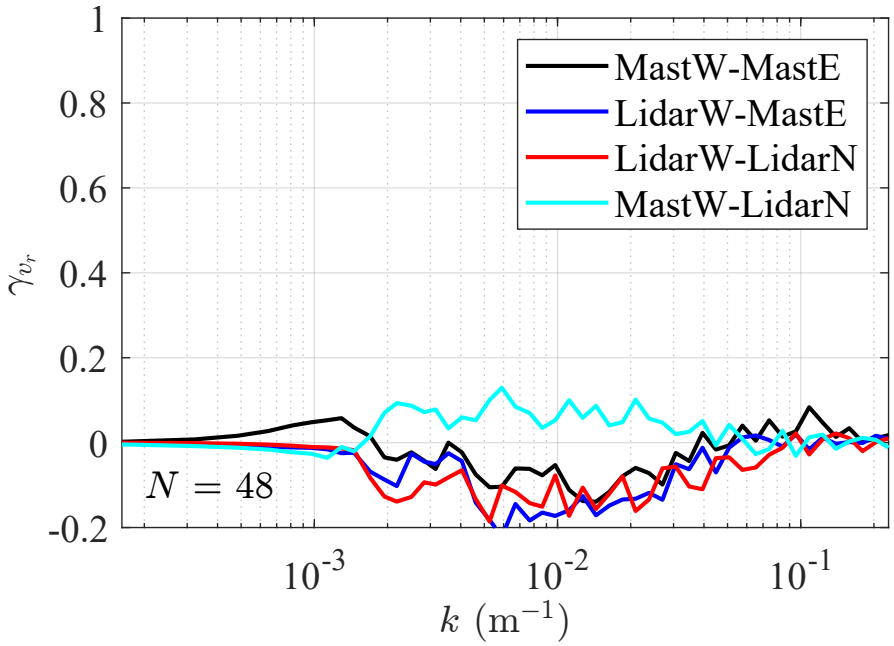

Figure 6.6: Later quad-coherence γ_{v_r} for along beam velocity component $\overline{v_r}$ measured for all wind directions (0° to 360°).

Bibliography

Alcayaga, L. (2020). Filtering of pulsed lidar data using spatial information and a clustering algorithm. *Atmospheric Measurement Techniques*, *13*, 6237–6254.

Axaopoulos, P. J., & Tzanes, G. T. (2022). Wind energy potential (measurements, evaluation, forecasting), .

Bechmann, A., Sørensen, N. N., Berg, J., Mann, J., & Réthoré, P.-E. (2011). The bolund experiment, part ii: blind comparison of microscale flow models. *Boundary-layer meteorology*, *141*, 245–271.

Berg, J., Mann, J., Bechmann, A., Courtney, M., & Jørgensen, H. E. (2011). The bolund experiment, part i: flow over a steep, three-dimensional hill. *Boundary-layer meteorology*, *141*, 219–243.

Bietry, J., Delaunay, D., & Conti, E. (1995). Comparison of full-scale measurement and computation of wind effects on a cable-stayed bridge. *Journal of wind engineering and industrial aerodynamics*, *57*, 225–235.

Bjørkhaug, B., & Poulsson, S. (1986). *Norges fyr: Fra svenskegrensen til Stad*. Grøndahl.

Boquet, M., Parmentier, R., & Cariou, J. (2010). Correction of pulsed wind lidars bias in complex terrain. ISARS.

Bosch, J., Staffell, I., & Hawkes, A. D. (2018). Temporally explicit and spatially resolved global offshore wind energy potentials. *Energy*, *163*, 766–781.

Brook, R. (1975). A note on vertical coherence of wind measured in an urban boundary layer. *Boundary-Layer Meteorology*, *9*, 11–20.

Carter, G., Knapp, C., & Nuttall, A. (1973). Estimation of the magnitude-squared coherence function via overlapped fast fourier transform processing. *IEEE transactions on audio and electroacoustics*, *21*, 337–344.

Chanin, M.-L., Garnier, A., Hauchecorne, A., & Porteneuve, J. (1989). A doppler lidar for measuring winds in the middle atmosphere. *Geophysical research letters*, *16*, 1273–1276.

Cheynet, E. (2016). *Wind-induced vibrations of a suspension bridge*. Ph.D. thesis University of Stavanger, Norway.

Cheynet, E., Flügge, M., Reuder, J., Jakobsen, J. B., Heggelund, Y., Svardal, B., Saavedra Garfias, P., Obhrai, C., Daniotti, N., Berge, J. et al. (2021). The cotur project: remote sensing of offshore turbulence for wind energy application. *Atmospheric Measurement Techniques*, *14*, 6137–6157.

Cheynet, E., Jakobsen, J., Snæbjörnsson, J., Ágústsson, H., & Harstveit, K. (2018a). Complementary use of wind lidars and land-based met-masts for wind measurements in a wide fjord. In *Journal of Physics: Conference Series* (p. 012028). IOP Publishing volume 1104.

Cheynet, E., Jakobsen, J. B., & Obhrai, C. (2017a). Spectral characteristics of surface-layer turbulence in the North Sea. *Energy Procedia*, *137*, 414–427.

Cheynet, E., Jakobsen, J. B., & Reuder, J. (2018b). Velocity spectra and coherence estimates in the marine atmospheric boundary layer. *Boundary-layer meteorology*, *169*, 429–460.

Cheynet, E., Jakobsen, J. B., Snæbjörnsson, J., Mann, J., Courtney, M., Lea, G., & Svardal, B. (2017b). Measurements of surface-layer turbulence in a wide norwegian fjord using synchronized long-range doppler wind lidars. *Remote Sensing*, *9*, 977.

Cheynet, E., Jakobsen, J. B., Snæbjörnsson, J., Mikkelsen, T., Sjöholm, M., Mann, J., Hansen, P., Angelou, N., & Svardal, B. (2016). Application of short-range dual-doppler lidars to evaluate the coherence of turbulence. *Experiments in Fluids*, *57*, 1–17.

Commission, I. E. et al. (2005). Wind turbines-part 1: design requirements. *IEC 61400-1-Ed. 3.0*, .

Davenport, A. G. (1961). The spectrum of horizontal gustiness near the ground in high winds. *Quarterly Journal of the Royal Meteorological Society*, *87*, 194–211.

Doubrawa, P., Churchfield, M. J., Godvik, M., & Sirnivas, S. (2019). Load response of a floating wind turbine to turbulent atmospheric flow. *Applied Energy*, *242*, 1588–1599.

D'Errico, J. (2017). inpaint_nans, version 1.1. 0.0.

Etienne Cheynet, J. B. J. (2022). Lecture notes in wind load on structures. part 1.

Frank, H. P. (1996). A simple spectral model for the modification of turbulence in flow over gentle hills. *Boundary-layer meteorology*, *79*, 345–373.

Frost, W., Long, B., & Turner, R. E. (1978). *Engineering handbook on the atmospheric environmental guidelines for use in wind turbine generator development*. Technical Report.

Hardesty, R., & Weber, B. (1987). Lidar measurement of turbulence encountered by horizontal-axis wind turbines. *Journal of Atmospheric and Oceanic Technology*, *4*, 191–203.

Hertwig, D., Gough, H. L., Grimmond, S., Barlow, J. F., Kent, C. W., Lin, W. E., Robins, A. G., & Hayden, P. (2019). Wake characteristics of tall buildings in a realistic urban canopy. *Boundary-Layer Meteorology*, *172*, 239–270.

Jelalian, A. V. (1992). *Laser radar systems*. Artech House on Demand.

Kaimal, J. C., & Finnigan, J. J. (1994). *Atmospheric boundary layer flows: their structure and measurement*. Oxford university press.

Kaimal, J. C., Wyngaard, J., Izumi, Y., & Coté, O. (1972). Spectral characteristics of surface-layer turbulence. *Quarterly Journal of the Royal Meteorological Society*, *98*, 563–589.

Kareem, A., & Tamura, Y. (2013). *Advanced structural wind engineering* volume 482. Springer.

Klein, E. (1948). Some background history of ultrasonics. *The Journal of the Acoustical Society of America*, *20*, 601–604.

Kolmogorov, A. N. (1941). The local structure of turbulence in incompressible viscous fluid for very large reynolds number. In *Dokl. Akad. Nauk. SSSR* (pp. 301–303). volume 30.

Krishnamurthy, R., Choukulkar, A., Calhoun, R., Fine, J., Oliver, A., & Barr, K. (2013). Coherent doppler lidar for wind farm characterization. *Wind Energy*, *16*, 189–206.

Kristensen, L., & Jensen, N. (1979). Lateral coherence in isotropic turbulence and in the natural wind. *Boundary-Layer Meteorology*, *17*, 353–373.

Kristensen, L., & Kirkegaard, P. (1986). *Sampling problems with spectral coherence* volume 526. Risø National Laboratory Roskilde, Denmark.

Kumer, V.-M., Reuder, J., & Furevik, B. R. (2014). A comparison of lidar and radiosonde wind measurements. *Energy Procedia*, *53*, 214–220.

Lange, J., Mann, J., Angelou, N., Berg, J., Sjöholm, M., & Mikkelsen, T. (2016). Variations of the wake height over the bolund escarpment measured by a scanning lidar. *Boundary-Layer Meteorology*, *159*, 147–159.

Larsén, X. G., & Mann, J. (2006). The effects of disjunct sampling and averaging time on maximum mean wind speeds. *Journal of wind engineering and industrial aerodynamics*, *94*, 581–602.

LUMLEY, J., & PANOFSKY, H. (1964). The structure of atmospheric turbulence(book on structure of atmospheric turbulence including basic characteristics and recent observations). *NEW YORK, INTERSCIENCE PUBLISHERS, 1964. 239 P*, .

Ma, Y., & Liu, H. (2017). Large-eddy simulations of atmospheric flows over complex terrain using the immersed-boundary method in the weather research and forecasting model. *Boundary-layer meteorology*, *165*, 421–445.

Macdonald, J. H. (2003). Evaluation of buffeting predictions of a cable-stayed bridge from full-scale measurements. *Journal of wind engineering and industrial aerodynamics*, *91*, 1465–1483.

Mahalanobis, P. C. (2018). On the generalized distance in statistics. *Sankhyā: The Indian Journal of Statistics, Series A (2008-)*, *80*, S1–S7.

Mann, J., Cariou, J.-P., Courtney, M. S., Parmentier, R., Mikkelsen, T., Wagner, R., Lindelow, P., Sjoholm, M., & Enevoldsen, K. (2009). Comparison of 3d turbulence measurements using three staring wind lidars and a sonic anemometer. *Meteorologische Zeitschrift*, *18*, 135.

McMillen, R. T. (1988). An eddy correlation technique with extended applicability to non-simple terrain. *Boundary-Layer Meteorology*, *43*, 231–245.

Midjiyawa, Z., Cheynet, E., Reuder, J., Ágústsson, H., & Kvamsdal, T. (2021a). Potential and challenges of wind measurements using met-masts in complex topography for bridge design: Part i–integral flow characteristics. *Journal of Wind Engineering and Industrial Aerodynamics*, *211*, 104584.

Midjiyawa, Z., Cheynet, E., Reuder, J., Ágústsson, H., & Kvamsdal, T. (2021b). Potential and challenges of wind measurements using met-masts in complex topography for bridge design: Part ii–spectral flow characteristics. *Journal of Wind Engineering and Industrial Aerodynamics*, *211*, 104585.

Miyata, T., Yamada, H., Katsuchi, H., & Kitagawa, M. (2002). Full-scale measurement of akashi–kaikyo bridge during typhoon. *Journal of wind engineering and industrial aerodynamics*, *90*, 1517–1527.

Monin, A. S., & Obukhov, A. M. (1954). Basic laws of turbulent mixing in the surface layer of the atmosphere. *Contributions to Geophysics and Geodesy of the Geophysical Institute, Academy of Sciences of the USSR*, *151*, e187.

Nybø, A., Nielsen, F. G., Reuder, J., Churchfield, M. J., & Godvik, M. (2020). Evaluation of different wind fields for the investigation of the dynamic response of offshore wind turbines. *Wind Energy*, *23*, 1810–1830.

Olesen, H., Larsen, S. E., & Højstrup, J. (1984). Modelling velocity spectra in the lower part of the planetary boundary layer. *Boundary-Layer Meteorology*, *29*, 285–312.

Panofsky, H., Larko, D., Lipschut, R., Stone, G., Bradley, E., Bowen, A. J., & Højstrup, J. (1982). Spectra of velocity components over complex terrain. *Quarterly Journal of the Royal Meteorological Society*, *108*, 215–230.

Panofsky, H. A., & Dutton, J. A. (1984). Atmospheric turbulence. models and methods for engineering applications, .

Panofsky, H. A., & McCormick, R. A. (1954). Properties of spectra of atmospheric turbulence at 100 metres. *Quarterly Journal of the Royal Meteorological Society*, *80*, 546–564.

Pauliac, R. (2009). Windcube user's manual. URL: https://breeze.colorado.edu/ATOC6020/2018_Spring_files/WLS7_UserManual_01rev01.pdf.

Pearson, G., Davies, F., & Collier, C. (2009). An analysis of the performance of the ufam pulsed doppler lidar for observing the boundary layer. *Journal of Atmospheric and Oceanic Technology*, *26*, 240–250.

Peña, A., Bay Hasager, C., & Lange, J. (2013). Remote sensing for wind energy, .

Peña, A., Dellwik, E., & Mann, J. (2019). A method to assess the accuracy of sonic anemometer measurements. *Atmospheric Measurement Techniques*, *12*, 237–252.

Pielke, R., & Panofsky, H. (1970). Turbulence characteristics along several towers. *Boundary-Layer Meteorology*, *1*, 115–130.

Rodrigo, P. J., & Pedersen, C. (2015). Direct detection doppler lidar using a scanning fabry-perot interferometer and a single-photon counting module. In *The European Conference on Lasers and Electro-Optics* (p. CH_P_15). Optica Publishing Group.

Ropelewski, C. F., Tennekes, H., & Panofsky, H. (1973). Horizontal coherence of wind fluctuations. *Boundary-Layer Meteorology*, *5*, 353–363.

Saranyasoontorn, K., Manuel, L., & Veers, P. S. (2004). A comparison of standard coherence models for inflow turbulence with estimates from field measurements. *J. Sol. Energy Eng.*, *126*, 1069–1082.

Slinger, C., & Harris, M. (2012). Introduction to continuous-wave doppler lidar. *Summer School in Remote Sensing for Wind Energy, Boulder, USA*, *11*.

Smalikho, I. (1995). On measurement of the dissipation rate of the turbulent energy with a cw doppler lidar. *Atmospheric and oceanic optics c/c of optika atmosfery i okeana*, *8*, 788–793.

Smith, S. D. (1980). Wind stress and heat flux over the ocean in gale force winds. *Journal of Physical Oceanography*, *10*, 709–726.

Solari, G., & Piccardo, G. (2001). Probabilistic 3-D turbulence modeling for gust buffeting of structures. *Probabilistic Engineering Mechanics*, *16*, 73–86.

Soucy, R., Woodward, R., & Panofsky, H. (1982). Vertical cross-spectra of horizontal velocity components at the boulder observatory. *Boundary-Layer Meteorology*, *24*, 57–66.

for Standardization, E. C. (2004). Eurocode 1: actions on structures—general actions—part 1-4: Wind actions, .

Stickland, M. (2012). International standard iec61400-12-1: Wind turbines-part 12-1: Power performance measurements of electricity producing wind turbines: Annex g, .

STN, E. (1991). 2: Eurocode 1: Actions on structures. *Part 2: Traffic loads on bridges*, .

Stull, R. B. (1988). *An introduction to boundary layer meteorology* volume 13. Springer Science & Business Media.

Taylor, G. I. (1938). The spectrum of turbulence. *Proceedings of the Royal Society of London. Series A-Mathematical and Physical Sciences*, *164*, 476–490.

Teunissen, H. (1980). Structure of mean winds and turbulence in the planetary boundary layer over rural terrain. *Boundary-Layer Meteorology*, *19*, 187–221.

Tieleman, H. W. (1995). Universality of velocity spectra. *Journal of Wind Engineering and Industrial Aerodynamics*, *56*, 55–69.

Tong, C. (1996). Taylor's hypothesis and two-point coherence measurements. *Boundary-layer meteorology*, *81*, 399–410.

Valldecabres, L., Peña, A., Courtney, M., von Bremen, L., & Kühn, M. (2018). Very short-term forecast of near-coastal flow¡? xmltex\break?¿ using scanning lidars. *Wind energy science*, *3*, 313–327.

Vaughan, J., & Forrester, P. (1989). Laser doppler velocimetry applied to the measurement of local and global wind. *Wind Engineering*, (pp. 1–15).

Veers, P. (1984). Modeling stochastic wind loads on vertical axis wind turbines. In *25th Structures, Structural Dynamics and Materials Conference* (p. 910).

Veers, P., Dykes, K., Lantz, E., Barth, S., Bottasso, C., Carlson, O., Clifton, A., Green, J., Green, P., Holttinen, H. et al. (2019). Grand challenges in the science of wind energy, science, 366, eaau2027.

Wang, H., Wu, T., Tao, T., Li, A., & Kareem, A. (2016). Measurements and analysis of non-stationary wind characteristics at sutong bridge in typhoon damrey. *Journal of Wind Engineering and Industrial Aerodynamics*, *151*, 100–106.

Weber, R. O. (1999). Remarks on the definition and estimation of friction velocity. *Boundary-Layer Meteorology*, *93*, 197–209.

Welch, P. (1967). The use of fast fourier transform for the estimation of power spectra: a method based on time averaging over short, modified periodograms. *IEEE Transactions on audio and electroacoustics*, *15*, 70–73.

Werner, C. (2005). Doppler wind lidar—range-resolved optical remote sensing of the atmosphere. *by DC Weitkamp. Springer*, (pp. 325–354).

Wilczak, J. M., Oncley, S. P., & Stage, S. A. (2001). Sonic anemometer tilt correction algorithms. *Boundary-layer meteorology*, *99*, 127–150.

Zeman, O., & Jensen, N. O. (1987). Modification of turbulence characteristics in flow over hills. *Quarterly Journal of the Royal Meteorological Society*, *113*, 55–80.